Control and Robustness Analysis for a High-α Maneuverable Thrust-Vectoring Fighter Aircraft

Özgür Atesoglu[*]
Aselsan, Inc., 06750 Ankara, Turkey
and
M. Kemal Özgören[†]
Middle East Technical University, 06531 Ankara, Turkey

This study focuses on designing a nonlinear controller for high-α maneuvers of a fighter aircraft with a thrust-vectoring control ability and checking the robustness of the designed controller using the structured singular-value μ-based robustness analysis. The controller is designed using the nonlinear dynamic inversion method. It is designed to engage either the aerodynamic control surfaces or the thrust-vectoring control paddles of the engines, depending on the flight conditions. The necessary mathematical models are built to describe the nonlinear flight dynamics, the nonlinear aerodynamics, the engine with thrust-vectoring paddles, and the aircraft sensors. The robustness analysis is especially needed when thrust-vectoring control is engaged in a challenging high-α maneuver. This is necessary to analyze the effect of increasing uncertainty in the aerodynamic parameters in such a flight condition. In a flight with thrust-vectoring control, the effect of the aerodynamic uncertainties on the robustness is investigated for two different cases. In the first case, the aerodynamic forces and moments are treated as if they are completely unknown. This unusual uncertainty assumption is proposed and investigated for the first time in this paper. In the second case, the aerodynamic forces and moments are assumed to be known but only with a limited degree of confidence (e.g., 70%). The results of the robustness analysis for each case show that it is impossible to achieve a satisfactory robustness if the aerodynamic forces and moments are treated as completely unknown disturbances, whereas robustness can be achieved rather easily if they are known even with only 70% confidence. These conclusions are also verified with numerical flight simulations.

Nomenclature

C_i	=	general symbol for the aerodynamic force/moment coefficients
$C_{n\beta dyn}$	=	dynamic sensitivity of yaw moment to sideslip angle
$\hat{C}^{(o,b)}$	=	rotation matrix from Earth-fixed reference frame to body-fixed reference frame
$\bar{F}_L, \bar{F}_R$	=	column matrix representations of the thrust force vectors of the left and right engines
$\bar{F}_a, \bar{M}_a$	=	column matrix representations of the aerodynamic force and moment vectors
$\hat{F}_u$	=	upper linear fractional transformation representation of a structured system
$\hat{G}_{\text{nom}}(s), \hat{G}(s)$	=	nominal and perturbed transfer matrices used in robustness analysis
$\bar{H}_e^{(b)}$	=	array of engine angular momentum components
$\hat{J}$	=	inertia matrix of the aircraft
J_e	=	inertia of the rotating machinery of the aircraft engines
$\hat{K}_p, \hat{K}_i, \hat{K}_d$	=	controller matrix gains
$\bar{M}_e^{(b)}$	=	array of engine moment components
p, q, r	=	angular velocity components of the aircraft in the body-fixed frame
$\hat{R}_k(\theta)$	=	rotation matrix of angle θ about the kth axis of a reference frame
$\bar{r}_{be_L}, \bar{r}_{be_R}$	=	column matrix representations of the position vectors of the engine nozzle exits
T_L, T_R	=	total thrust forces created by the left and right aircraft engines
$T_{\text{mil}}, T_{\text{idle}}, T_{\text{max}}$	=	military, idle, and maximum thrust levels
u, v, w	=	translational velocity components of the aircraft in the body-fixed frame
V_T, α, β	=	total velocity, angle of attack, and sideslip angle
$\bar{X}, \tilde{X}$	=	column matrix representation and cross-product matrix of a vector $\mathbf{X}$
$\hat{\Delta}$	=	matrix representation of the uncertain model perturbations
$\Delta\hat{G}(s)$	=	additive uncertainty transfer matrix used in the robustness analysis
$\delta_{L(1,2,3)}, \delta_{R(1,2,3)}$	=	left and right engine thrust-vectoring paddle deflections
$\delta_{Lth}, \delta_{Rth}$	=	left and right engine throttle deflections
$\delta_a, \delta_e, \delta_r$	=	aileron, elevator, and rudder deflections
$\mu(\hat{M})$	=	structured singular value of a system realization matrix $\hat{M}$
ψ, θ, ϕ	=	Euler angles describing the attitude of the aircraft
ψ_L, θ_L	=	azimuth and elevation deviations of the thrust vector of the left engine
ψ_R, θ_R	=	azimuth and elevation deviations of the thrust vector of the right engine
$\bar{\omega}_{b/o}$	=	column matrix representation of the angular velocity vector of the aircraft
ω_e	=	angular velocity of the rotating machinery of the aircraft engine
$\omega_{ni}, \zeta_i, \omega'_{ni}$	=	control parameters of the desired closed-loop dynamics

[*]Lead Design Engineer, Navigation and Guidance Systems Department, Microelectronics, Guidance, and Electro-Optics Division. Member AIAA.
[†]Professor, Mechanical Engineering Department.

I. Introduction

THE basic flight maneuvers of the air-superiority fighters are mostly executed at high-angle-of-attack flight regimes. This is generally necessary to successfully defend against adversary fighters. The high-angle-of-attack aerodynamics are inherently associated with separated flows and nonlinear aerodynamics [1]. Resistance to departure from the controlled flight, ability to control the aircraft at high-angle-of-attack combat maneuvers, and allowance for unlimited angle-of-attack range are the major concerns that a supermaneuverable fighter should have. There are certain requirements for fighters that they should be able to perform velocity vector roll [2,3], Cobra [4,5], and Herbst [6–8] maneuvers and realize a nose pointing (or cueing) maneuver to allow a missile lock-on and fire. Thus, the demand for increased agility and maneuvering has led to the necessity of high-angle-of-attack flight. This necessity in turn has led to the development of agile and supermaneuverable aircraft such as Harrier AV-8, Yakovlev Yak-141, Sukhoi Su-27, Su-37, F-35B, and F-22. On the other hand, the demand for increased agility and maneuverability has also led to the development of research programs such as X-31A enhanced fighter maneuverability [9,10], F-16 multi-axis thrust vectoring [11], X-29A vortex flight control system [12], and NASA High-Alpha Technology Program [13].

During rapid high-angle-of-attack maneuvers, unsteady aerodynamic effects (which have a crucial impact on the aircraft flight dynamics, including stability and control) are extremely important. Because the aircraft is operating at highly nonlinear flow regimes with substantial angular rates, the prediction of departures from a stall-safe flight and the related complex dynamics should receive increased attention. Several studies exist in this area, including development of guidelines for preliminary design [14], improved testing techniques [15], and improved analysis techniques (e.g., prediction of falling-leaf motions) [16], and simulation-based predictive capabilities [17].

The aim of the designed controller, which is presented in this paper, is to enhance the rapid maneuvering capability of the aircraft in the high-angle-of-attack flight and to bring the capability to make automated rapid maneuvers in that flight regime. Hence, the aircraft will have considerable tactical advantages by the automated and enhanced poststall capability in air-to-air combat. However, as mentioned earlier, as the aircraft operate at highly nonlinear flow regimes, the aircraft dynamics become more nonlinear, uncertain, unstable, and unpredictable. Hence, designing flight control laws for poststall flight at high angles of attack is a challenging task. Here, the nonlinearities typically arise from both the aerodynamics and the inertial coupling terms [18–20].

The conventional approach to designing a flight control law for operations in a wide envelope is to schedule the controller gains as functions of slow-varying entities such as V_T, h, α, β, etc. Nevertheless, gain scheduling with respect to rapidly changing variables (such as α, ϕ, and θ) can often lead to stability and performance problems at high angles of attack. Furthermore, designing the gain-scheduling schemes and tuning them are quite difficult and time-consuming [21,22].

In this paper, the controller design is based on the nonlinear dynamic inversion (NDI) technique. This technique uses the control inputs to cancel out the nonlinear state equations and replace them with desirable linear equations. Thus, it becomes possible to control a nonlinear system without requiring its linearized model. The inversion transformation provides an inherent gain scheduling, and this eliminates a tedious gain-scheduling procedure to be developed for the linearized model [23,24]. The NDI technique is simple in principle, but in the case of flight control, the system to be inverted is generally underactuated and thus not invertible. As a remedy, an effective method known as time-scale separation is developed to skip such singularity problems and applied successfully, together with NDI controllers [25–31]. In Sec. II, brief explanations are given about the NDI technique, the time-scale separation method, and the assignment of the inverted plant dynamics as desired. Although NDI is quite an effective controller design technique, it is very sensitive to uncertainties and unmodeled features of the plant dynamics and

therefore does not readily guarantee the robustness of the closed-loop system. This necessitates that it must be accompanied by a robustness analysis. A brief explanation about the robustness issues is also given in Sec. II.

The present study starts with the modeling of the aircraft dynamics. The effect of the rotating engine parts is also included in the modeling. Then the detailed modeling of the aerodynamic forces and moments, the engine thrust, and the aerodynamic and thrust control effectors are presented, together with the dynamic and error models of the onboard sensors.

To achieve the desired automated maneuvers, the attitude angles of the aircraft are to be controlled. For this purpose, both the aerodynamic and the thrust-vectoring control effectors can be used in a properly sequenced manner. The sequence is arranged so that the aerodynamic control is switched on during an ordinary flight phase, but the thrust-vectoring control (TVC) is switched on when the aerodynamic control becomes ineffective for a critical maneuver. As a part of the control process, the desired forces and moments are computed using the specified values of the desired accelerations. Then the desired deflections of the control effectors (i.e., the aerodynamic control surfaces or the TVC paddles) are determined corresponding to the computed desired forces and moments.

Finally, the robust performance analysis is carried out for the proposed controller. The details of this analysis can be seen in Sec. V. In this analysis, the effects of the aerodynamic uncertainties are analyzed for two different cases. In the first case, the aerodynamic coefficients are treated as if they are completely unknown (i.e., as if they have 0% certainty). This unusual assumption is proposed and investigated for the first time in this paper. In the second case, the aerodynamic coefficient model accuracy is maintained at a certain level and the robustness analysis is repeated. Afterward, the stability and performance of the proposed controller is verified by means of a numerical simulation of a selected high-α maneuver. The results show that the designed controller can be stable and robust if the confidence level of the aerodynamic uncertainties is above a certain minimum.

II. Nonlinear-Dynamic-Inversion-Based Flight Control

The first step in any aircraft control law design is to determine the required forces and moments that are expected to be realized by the control effectors. This can be done by using the NDI approach [25–28]. This approach depends on the direct manipulation of the equations of motion to cancel out the nonlinear terms in the dynamic equations and generate control laws yielding the desired responses for the achievement of the desired maneuvers. The controlled outputs are generally taken as the body angular rates. However, the angle of attack and the sideslip angle are also carefully monitored.

The NDI technique is used extensively in designing flight control systems [22–31]. This controller design technique uses the information about the nonlinear dynamics of the aircraft. The resulting nonlinear controller becomes valid for the whole flight envelope, and therefore there is no need to apply any gain scheduling. Other important features of this design technique can be stated as the decoupling of the longitudinal dynamics from the lateral dynamics even at a high-α flight [29], the independent assignment of the closed-loop dynamics for each output channel, and the convenience of designing simple and conventional controllers for the decoupled output channels.

A. Time-Scale Separation Method

Even though the basic dynamic inversion process is simple, in flight control problems, the number of the state variables to be controlled is generally larger than the number of the control variables; that is, the system is underactuated and thus is not invertible. To bypass this singularity of dynamic inversion, the time-scale separation method can be used as a remedy. This method is explained subsequently.

In the aircraft control literature, because the control effectiveness on the angular variables ($\psi, \theta, \phi, \alpha, \beta$) is rather low, they are considered as the slow dynamics variables. On the other hand, the

control effectiveness on the angular velocity components (p, q, r) is comparatively higher, and therefore they are considered as the fast dynamics variables. The separation of the fast and slow dynamics is generally known as the two-time-scale separation method. A system that is separable this way (i.e., an aircraft) can be represented by the following kinds of two generic differential equations such that the control input appears in only one of them:

$$\dot{\bar{x}}_1 = \bar{f}_1(\bar{x}_1) + \hat{B}_1(\bar{x}_1)\bar{x}_2 \tag{1a}$$

$$\dot{\bar{x}}_2 = \bar{f}_2(\bar{x}_1, \bar{x}_2) + \hat{B}_2(\bar{x}_1, \bar{x}_2)\bar{u} \tag{1b}$$

To control the generic system shown previously, as the first step, for a desired value $\bar{x}_{1d}$ of $\bar{x}_1$, the commanded value of the time rate of change of $\bar{x}_1$ ($\dot{\bar{x}}_{1c}$) is calculated. This operation is shown in the s domain as

$$s\bar{X}_{1c}(s) = \hat{G}_1(s)[\bar{X}_{1d}(s) - \bar{X}_1(s)]$$

Here, $\hat{G}_1(s)$ is the controller transfer matrix to be generated for the slow dynamics represented by Eq. (1a). Then $\dot{\bar{x}}_{1c}$ is used to calculate the desired value $\bar{x}_{2d}$ of $\bar{x}_2$ as

$$\bar{x}_{2d} = \hat{B}_1^{-1}(\bar{x}_1)[\dot{\bar{x}}_{1c} - \bar{f}_1(\bar{x}_1)]$$

provided that $\hat{B}_1(\bar{x}_1)$ is not singular. As the second step, the commanded value of the time rate of change of $\bar{x}_2$ ($\dot{\bar{x}}_{2c}$) is calculated. This is shown in the s domain as

$$s\bar{X}_{2c}(s) = \hat{G}_2(s)[\bar{X}_{2d}(s) - \bar{X}_2(s)]$$

Here, $\hat{G}_2(s)$ is the controller transfer matrix to be generated for the fast dynamics represented by Eq. (1b). Finally, $\dot{\bar{x}}_{2c}$ is used to calculate the control input $\bar{u}$ as

$$\bar{u} = \hat{B}_2^{-1}(\bar{x}_1, \bar{x}_2)[\dot{\bar{x}}_{2c} - \bar{f}_2(\bar{x}_1, \bar{x}_2)]$$

provided that $\hat{B}_2(\bar{x}_1, \bar{x}_2)$ is not singular or ill-conditioned. This control method is illustrated in Fig. 1.

B. Assignment of the Desired Dynamics to the Closed-Loop System

The controller transfer matrices define the desired dynamics of the closed-loop system controlled by using the NDI technique. Because of the closed-loop performance requirements and varying plant characteristics, different desired dynamics assignments can be enforced in the design approach. Generally, the desired closed-loop dynamics are formed by using the proportional (P) and the proportional with integral (PI) control schemes [27–31].

In the P control scheme, considering a first-order system as an example, the time rate of change of the controlled variable x is assigned to the desired dynamics as $\dot{x}_c = k_p(x_d - x)$. Here, k_p sets the bandwidth of the closed-loop response by placing a single pole (at $s = -k_p$) for the closed-loop transfer function. The closed-loop transfer function bandwidth must be selected to satisfy the specified closed-loop performance requirements and must not exceed the

physical capabilities (limits on position, rate, power, etc.) of the control actuator.

If the P control law cannot create satisfactory closed-loop control performance, then a higher-order control law can be used. In the NDI applications, a commonly used higher-order control law is PI. It is particularly popular in the NDI literature concerned with fighter aircraft examples [30]. In this case, considering the previous example again, the time rate of change of the controlled variable x is assigned to the desired dynamics as

$$\dot{x}_c = k_p(x_d - x) + k_i \int_0^t (x_d - x)d\tau$$

Here, k_p and k_i set the bandwidth and damping properties of the closed-loop response by placing complex conjugate pole pairs at

$$s_{1,2} = -\omega_{nd}\xi_d \pm j\omega_{nd}(1 - \xi_d^2)^{1/2}$$

for the closed-loop transfer function. Assigning desired values ξ_d and ω_{nd} to the damping ratio and the natural frequency of the closed-loop system, the controller gains can be calculated as $k_p = 2\xi_d\omega_{nd}$ and $k_i = \omega_{nd}^2$.

In the aeronautical control applications, the desired dynamics can also be specified in terms of the flying-quality and ride-quality levels [30]. MIL-STD-1797A [32] contains the flying-quality specifications for different vehicle classes and mission types. Based on this information, the proper time-domain characteristics corresponding to a desired flying-quality level (characterized by the damping ratio and the natural frequency of the closed-loop system) can be selected and the proper values for the control gains can be determined.

C. Robustness Analysis

Because the NDI controller design is based on canceling the nominal values of the nonlinear terms, it is very sensitive to the parameter uncertainties and the unmodeled dynamics. In other words, the robustness of the NDI-based control system may not be guaranteed in the presence of parameter uncertainties and unmodeled dynamics. Therefore, it is necessary to complement the nonlinear flight controller design process with the robustness analysis [33–35].

A control system is robust if it is insensitive to the differences between the actual system and the model of the system used to design the controller. These differences are generally referred to as the model-plant mismatch or the model uncertainty. Hence, to analyze the performance of the controlled system, the modeling uncertainties must be identified and their mathematical representations must be established. Then the stability and performance of the system can be checked to see whether they satisfy the robustness criteria.

Finding the H_∞ norm of a system and measuring the performance in terms of the calculated value brings certain advantages in dealing with the uncertainties in the system [36]. Denoting the open-loop plant matrix, without the uncertainties, with $\hat{P}$, the already synthesized controller matrix with $\hat{K}$, the controlled closed-loop system with $\hat{M}$, and the uncertain model perturbations with a block diagonal matrix $\hat{\Delta} = \text{diag}(\Delta_i)$, the robust performance analysis can be pursued as described subsequently by constructing the linear fractional transformation (LFT) structure of the controlled system
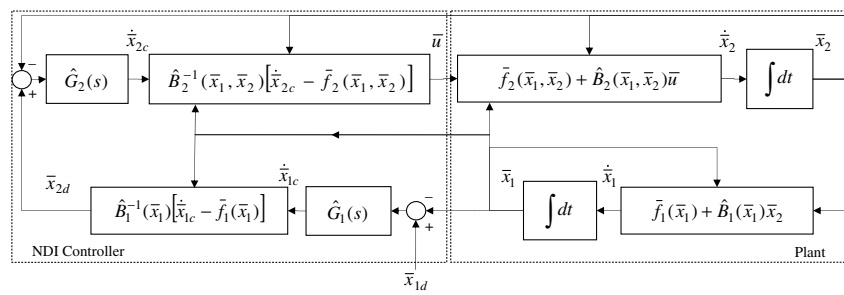

Fig. 1   Block diagram of a closed-loop system controlled by using NDI with time-scale separation.

Fig. 2 LFT block diagram.

Fig. 3 Definition of the forces, moments and vectors on the aircraft [41].
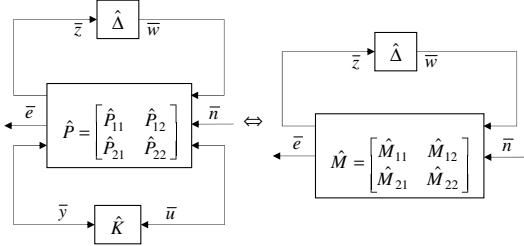
with parameter uncertainties. The LFT structure is illustrated in Fig. 2.

In Fig. 2, $\bar{n}$ is the noise or disturbance vector and $\bar{e}$ is the vector of the error signals. The error signals are generally chosen as the differences between the desired command values and the outputs of the system. However, it is possible that, due to the design considerations, they can be chosen as the differences between the outputs of the system and the outputs of the desired model plant subjected to the same inputs as the controlled plant. The vectors $\bar{w}$ and $\bar{z}$ define the signals between the system of uncertain model perturbations $\hat{\Delta}$ and the system. Here, if the aim is to design a robust controller, then the open-loop plant $\hat{P}$ is used in the LFT block diagram structure. On the other hand, if the aim is the robustness analysis of an already controlled system, then the closed-loop plant $\hat{M}$ (i.e., $\hat{P}$ controlled with $\hat{K}$) is chosen. To analyze the effects of the noise disturbance $\bar{n}$ and the parametric uncertainty $\bar{w}$ signals on the closed-loop system performance separately, the system matrix $\hat{M}$ can be decomposed into subsystem matrices by defining the upper LFT representation of $\hat{M}$ as

$$\hat{F}_u(\hat{M}, \hat{\Delta}) \triangleq \hat{M}_{22} + \hat{M}_{21}\hat{K}(\hat{I} - \hat{M}_{11}\hat{\Delta})^{-1}\hat{M}_{12}$$

The H_∞ analysis is very conservative for realistic problems with structured uncertainties, because the structure of the uncertainty block $\hat{\Delta}$ is not taken into account. Thus, to define a less conservative measure, the structured singular value μ is introduced [36–40], which is defined as

$$\mu(\hat{M}) \triangleq (\min\{\bar{\sigma}(\hat{\Delta}) | \det(\hat{I} - \hat{M}\hat{\Delta}) = 0 \quad \text{for structured } \hat{\Delta}\})^{-1}$$

Here, an exact solution for μ cannot be found, but approximate solutions can be found that constitute upper and lower bounds on μ. Solution methods that give upper bounds for μ are explained in detail in the literature [37–40].

To test the robust performance of an already controlled system, the uncertain controlled system is first arranged into a $\hat{F}_u(\hat{M}, \hat{\Delta})$ LFT structure such that $\|\hat{\Delta}\|_\infty \leq 1 \ \forall \ \omega$. Then, using the frequency response of the constructed LFT structure, the structured singular value of robust performance ($\mu_{\Delta RP}$) can be calculated. If the peak of $\mu_{\Delta RP}$ (i.e., μ_{peak}) across all frequencies is less than 1, then the $\hat{F}_u(\hat{M}, \hat{\Delta})$ system is said to satisfy the nominal performance, robust stability, and the robust performance [40].

III. Modeling the Fighter Aircraft

A. Modeling the Aircraft Dynamics

For the dynamic model of the fighter aircraft shown in Fig. 3, the model presented in a previous work of the authors [41] is used. Hence, the Newton–Euler equations describing the rigid-body motion of the aircraft can be combined into a single augmented matrix equation as

$$\begin{bmatrix} [\dot{u} & \dot{v} & \dot{w}]^T \\ [\dot{p} & \dot{q} & \dot{r}]^T \end{bmatrix} = \bar{F} + \hat{G}\begin{bmatrix} \bar{F}_L^{(b)} \\ \bar{F}_R^{(b)} \end{bmatrix} + \hat{H}\begin{bmatrix} \bar{F}_a^{(b)} \\ \bar{M}_a^{(b)} \end{bmatrix} \qquad (2)$$

Here, u, v, and w are the translational velocity components expressed in the body-fixed frame and p, q, and r are the angular velocity components expressed in the body-fixed reference frame. Also,
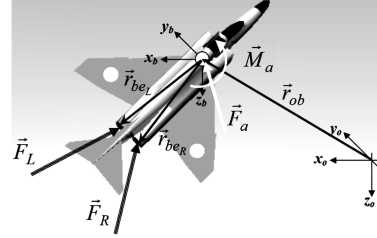
$$\bar{F}_L^{(b)} = T_L\hat{R}_3(\psi_L)\hat{R}_2(\theta_L)\bar{u}_1$$

and

$$\bar{F}_R^{(b)} = T_R\hat{R}_3(\psi_R)\hat{R}_2(\theta_R)\bar{u}_1$$

are the thrust force vectors with magnitudes T_L and T_R. The azimuth and elevation angles of $\bar{F}_L^{(b)}$ and $\bar{F}_R^{(b)}$ with respect to the body-fixed reference system are denoted by the pairs $\{\psi_L, \psi_R\}$ and $\{\theta_L, \theta_R\}$. The aerodynamic force and moment vector components expressed in the body-fixed frame, created on the aircraft during its flight, are denoted with $\bar{F}_a^{(b)}$ and $\bar{M}_a^{(b)}$. The locations of the thrust forces are denoted with respect to the origin of the body-fixed reference frame with the position vectors $\bar{r}_{be_L}$ and $\bar{r}_{be_R}$. The position of the aircraft with respect to the Earth-fixed reference frame is denoted with $\bar{r}_{ob}$.

The details of the matrices $\bar{F}$, $\hat{G}$, and $\hat{H}$ used in Eq. (2) are shown next:

$$\bar{F} = \begin{bmatrix} -\tilde{\omega}_{b/o}^{(b)}\bar{v}_{b/o}^{(b)} + g\hat{C}^{(b,o)}\bar{u}_3 \\ -\hat{J}^{-1}\tilde{\omega}_{b/o}^{(b)}\hat{J}\bar{\omega}_{b/o}^{(b)} \end{bmatrix}, \qquad \hat{G} = \begin{bmatrix} \hat{I}/m & \hat{I}/m \\ \hat{J}^{-1}\tilde{r}_{be_L}^{(b)} & \hat{J}^{-1}\tilde{r}_{be_R}^{(b)} \end{bmatrix}$$

$$\hat{H} = \begin{bmatrix} \hat{I}/m & 0 \\ 0 & \hat{J}^{-1} \end{bmatrix} \qquad (3)$$

Here, the mass of the aircraft is denoted with m, the inertia tensor of the aircraft is expressed by the matrix $\hat{J} = \hat{J}^{(b)}$ in the body-fixed frame, the gravitational acceleration is denoted with g, and $\hat{C}^{(b,o)}$ is the rotation matrix from the Earth-fixed reference frame to the body-fixed reference frame. It is expressed using the yaw–pitch–roll Euler angles (ψ, θ, ϕ). The translational velocity of the aircraft with respect to the Earth-fixed reference frame expressed in the body-fixed frame is denoted with $\bar{v}_{b/o}^{(b)}$, and the angular velocity of the aircraft with respect to the Earth-fixed reference frame expressed in the body-fixed frame is denoted with $\bar{\omega}_{b/o}^{(b)}$.

In this study, the dynamic model of the fighter aircraft is enhanced with respect to the model in [41] by adding the effect of the angular momentum, arising from the rotating parts of the engines spinning at high speeds. The resulting modified version of Eq. (2) is shown next:

$$\begin{bmatrix} [\dot{u} & \dot{v} & \dot{w}]^T \\ [\dot{p} & \dot{q} & \dot{r}]^T \end{bmatrix} = \hat{F} + \hat{G}\begin{bmatrix} \bar{F}_1^{(b)} \\ \bar{F}_2^{(b)} \end{bmatrix} + \hat{H}\begin{bmatrix} \bar{F}_a^{(b)} \\ \bar{M}_a^{(b)} \end{bmatrix}$$
$$+ \begin{bmatrix} \bar{0} \\ [\dot{p}_e & \dot{q}_e & \dot{r}_e]^T \end{bmatrix} \qquad (4)$$

Here, $[\dot{p}_e \quad \dot{q}_e \quad \dot{r}_e]^T$ arises due to the angular momentum $J_e\omega_e$ of the rotating engine parts and it is expressed as follows, assuming that ω_e varies slowly compared with the aircraft dynamics:

$$\begin{bmatrix} \dot{p}_e \\ \dot{q}_e \\ \dot{r}_e \end{bmatrix} = \hat{J}^{-1}\begin{bmatrix} 0 & -r & q \\ r & 0 & -p \\ -q & p & 0 \end{bmatrix}\begin{bmatrix} J_e\omega_e \\ 0 \\ 0 \end{bmatrix}$$
$$= \begin{bmatrix} -J_{xz}/(-J_xJ_z + J_{xz}^2)(qJ_e\omega_e) \\ (-1/J_y)(rJ_e\omega_e) \\ -J_x/(-J_xJ_z + J_{xz}^2)(qJ_e\omega_e) \end{bmatrix} \qquad (5)$$

It is obvious from Eq. (5) that the angular momentum originating from the rotating parts of the engines will induce undesired angular accelerations ($\dot{q}_e, \dot{r}_e$) on the axis perpendicular to the axis of instant motion (r, q). Hence, the pilot/autopilot will have more workload to suppress this undesirable disturbing effect during a maneuver.

B. Modeling the Aircraft Engines

Each engine of the aircraft is modeled as a first-order dynamic system with $\dot{P}_a = (1/\tau_{\mathrm{eng}})(P_c - P_a)$. Here, P_a is the actual power output and P_c is the commanded power demand. The engine time constant τ_{eng} is scheduled to achieve a satisfactory engine dynamics. $P_{c_{L,R}}$ are computed as functions of the throttle positions of the left and right engines ($\delta_{th_{L,R}}$). The resultant total thrust $T_{L,R}$ for the left or right engines of the aircraft can be estimated using the following approximate formula, which involves the idle, military, and maximum thrust values as functions of the Mach number, the altitude, and the actual power of the engine [41–43]:

$$P_{c_{L,R}}(\delta_{th_{L,R}}) = \begin{cases} (64.94)\delta_{th_{L,R}} & \text{if } \delta_{th_{L,R}} \leq 0.77 \\ (217.38)\delta_{th_{L,R}} - 117.38 & \text{if } \delta_{th_{L,R}} > 0.77 \end{cases} \quad (6)$$

$$T_{L,R}(M, h, P_{a_{L,R}}) =$$

$$\begin{cases} T_{\mathrm{idle}}(M,h) + (T_{\mathrm{mil}}(M,h) - T_{\mathrm{idle}}(M,h))(\frac{P_{a_{L,R}}}{50}) & \text{if } P_{a_{L,R}} < 50 \\ T_{\mathrm{mil}}(M,h) + (T_{\mathrm{max}}(M,h) - T_{\mathrm{mil}}(M,h))(\frac{P_{a_{L,R}}-50}{50}) & \text{if } P_{a_{L,R}} \geq 50 \end{cases}$$

$$(7)$$

The fighter aircraft considered in this study originally does not have the capability of thrust-vectoring. Thus, it is virtually fitted with a thrust-vectoring actuation system similar to those used in the X-31A and NASA F-18 HARV aircraft. It employs three radially displaced postexit vanes on each nozzle exit of the right and left engines. Therefore, thrusts of the right and left engines can be deviated individually. The details of the modeling and the hexagonal-shaped envelope generated to define the transformation between the thrust-vectoring paddle deflections and the resultant thrust deviation angles can be found in [41]. All three paddles of each engine are assumed to deflect 30 deg at most. The corresponding maximum values of the lateral $\psi_{L,R}$ and longitudinal $\theta_{L,R}$ thrust deviations are 30 and 20 deg, respectively. As for the mechanization of the three thrust-vectoring paddles, which are located at the nozzle exits of the engines, they are actuated independently. The actuator dynamics are modeled as a first-order system with a bandwidth frequency of $f_{nT} = 30$ Hz.

C. Modeling the Aerodynamics

In this study, the aerodynamic control of the aircraft is achieved with the elevator, aileron, and rudder deflections ($\delta_e, \delta_a, \delta_r$). The aerodynamic data [42] are constructed so that there is no ground effect, the landing gears are retracted, and there are no external stores. The aerodynamic coefficients ($C_x, C_y, C_z, C_l, C_m, C_n$) are built as functions of the angle of attack α, the sideslip angle β, the body angular velocity components (p, q, r), and the control surface deflections ($\delta_e, \delta_a, \delta_r$). The polynomial fits are computed separately for the regions $-15 \deg \leq \alpha \leq 15 \deg$, $15 \deg < \alpha < 30 \deg$, and $30 \deg \leq \alpha \leq 90 \deg$. Also, the yaw and pitch moment coefficients (C_n, C_m) are corrected with respect to the changing position of the center of gravity due to the fuel consumption during the flight. The aerodynamic control surfaces are limited to $-21 \deg \leq \delta_e \leq 7 \deg$, $-16 \deg \leq \delta_a \leq 16 \deg$, and $-30 \deg \leq \delta_r \leq 30 \deg$.

Using the aerodynamic data, a preanalysis of the stall tendency of the modeled aircraft is carried out by calculating the stall indication parameters $C_{n\beta dyn}$ and the lateral control departure parameter (LCDP). For a stall-safe region, both of these parameters shall have positive values. The expressions of the stall prediction parameters are given as

$$C_{n\beta\mathrm{dyn}} = C_{n\beta} \cos(\alpha) - (J_z/J_x)C_{l\beta} \sin(\alpha)$$

and

$$\mathrm{LCDP} = C_{n\beta} - C_{l\beta}(C_{n\delta_a}/C_{l\delta_a})$$

Here, $C_{n\beta}$ and $C_{l\beta}$ are the sensitivities of the yaw and roll moments to the sideslip angle, and J_z and J_x are the inertia components of the aircraft along the z and x axes of the body-fixed frame. The variations of $C_{n\beta\mathrm{dyn}}$ and LCDP vs α together with the Bihrle–Weissmann chart are shown in Fig. 4. When this figure is examined, for $p = r = \beta = 0$, the stall-free region is observed to be encountered for $-15 \deg \leq \alpha \leq 22 \deg$. Nevertheless, for $\alpha \geq 17 \deg$, weak spin resistance and roll reversals can be seen. As the angle of attack is increased further, the roll reversals and flow separation become
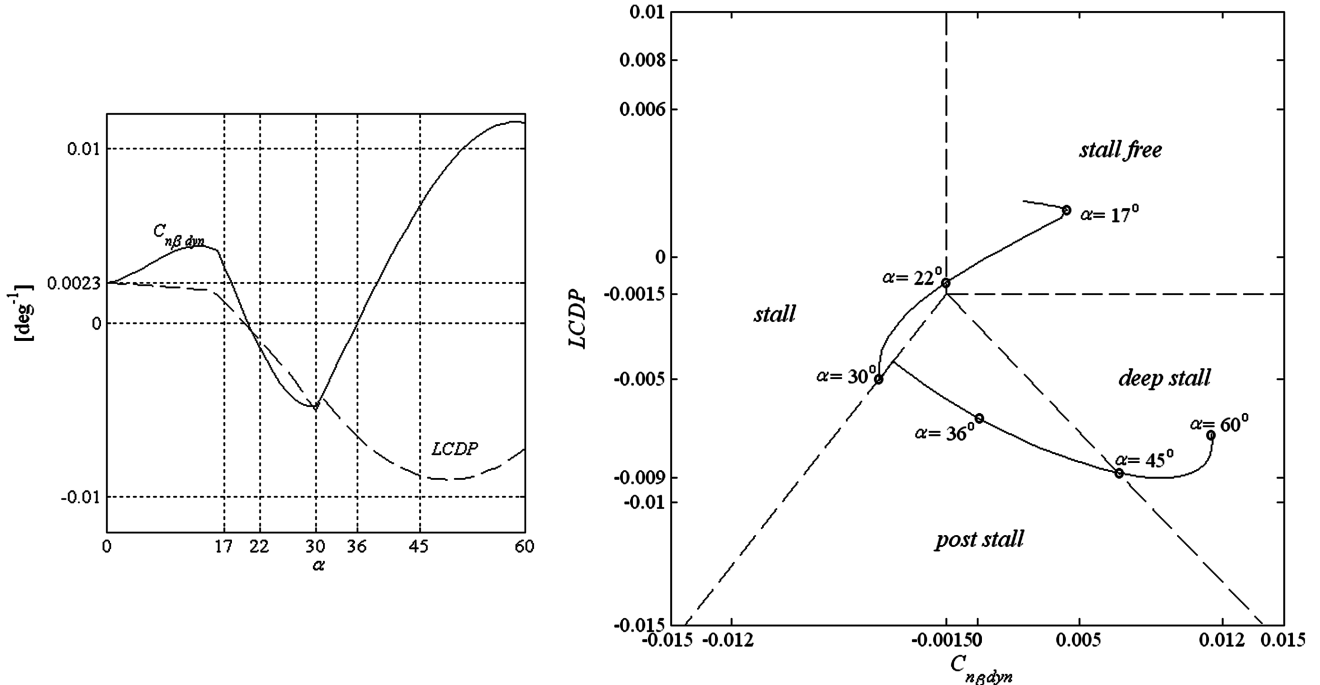

Fig. 4 $C_{n\beta dyn}$, **LCDP, and the integrated Bihrle–Weissmann chart for the fighter aircraft.**

effective and the control effectiveness decreases. The regions such that $30 \deg \leq \alpha \leq 45 \deg$ and $45 \deg \leq \alpha$ are counted as poststall and deep-stall regions.

D. Modeling the Aircraft Sensors

Because the dynamics and noise characteristics of the feedback sensors have a crucial part in the robustness analysis of the proposed controller, their models are also taken into account. In this study, models are built for the inertial navigation system (INS) and the set of sensors that constitute the inertial measurement unit (IMU).

The INS mainly consists of an IMU containing a cluster of sensors (three accelerometers and three gyroscopes) and a navigation computer. The inertial sensors are rigidly mounted to a common base within the IMU to maintain the same relative orientations. The navigation computer calculates the estimates of the attitude, velocity, and position of the host vehicle by integrating the angular velocity and translational acceleration information coming from the IMU. Although an INS is a preferable system because of being immune to jamming and inherently stealthy, due to the integration of the errors in the inertial sensors, the navigation errors grow with time. This is compensated by the usage of aiding sensors together with the inertial sensors. A modern fighter aircraft normally has a hybrid INS that is aided with other sensors such as a Global Positioning System, an altimeter, true airspeed sensors, a Doppler radar, etc. This brings the opportunity to suppress the growth of the navigation errors and limit them within certain bounds. This is typically done by fusing the information coming from the aiding sensors with the calculated navigation results and estimating the errors of the inertial sensors by applying Kalman filtering [44].

The errors of an INS have both deterministic and stochastic features caused by the operation principles of the inertial sensors of the IMU. The well-known errors are the bias, the instability of the bias, the scale factor, and the misalignment errors. However, the bias and the bias instability errors are more important than the others, because a notable amount of calibration work is normally done in the laboratories to eliminate the other errors before the products are released.

The measurement errors of the angular velocity components (p, q, r) with a gyroscope triad in an IMU can be modeled by using the bias and the bias instability errors. For example, the measurement of the roll rate gyroscope can be expressed as

$$p_m(t) = p(t) + b_p + n_p(t)$$

Here, b_p is the bias term, which is modeled to be constant, and $n_p(t)$ is the stochastic bias instability term, which is modeled as if it is generated using a first-order Gauss–Markov process as a shaping filter: that is, $T_p \dot{n}_p(t) + n_p(t) = w_p(t)$. Here, T_p is the time constant of the first-order Gauss–Markov process, and $w_p(t)$ is a white Gaussian noise [45]. The gyroscopes for the pitch and yaw rates (q and r) are also modeled to have similar error characteristics.

As mentioned before, the attitude is calculated by fusing the IMU and the aiding sensor measurements by means of a Kalman filter. Thus, the inertial sensors become calibrated in a sense and the navigation errors are maintained to be within tolerable finite bounds. Similar to the angular velocity measurements, these bounded errors on the attitude angles have both deterministic and stochastic features. Furthermore, it is obvious that the navigation and the filtering calculations take some time, and therefore the Euler angles become available with a time lag. This suggests that the attitude measurements should be modeled as the outcomes of conceptual sensors with first-order dynamics. For example, for the roll angle ϕ, the first-order sensor dynamics are expressed as $T_{\text{INS}} \dot{\phi}'(t) + \phi'(t) = \phi(t)$. Here, T_{INS} is the assumed time constant and $\phi'(t)$ is the lagged output. As for the error modeling, similar to the roll rate p measurement of the IMU, the roll angle measurement is expressed as $\phi_m(t) = \phi'(t) + b_\phi + n_\phi(t)$. Here, b_ϕ is the bias term, which is modeled to be constant, and $n_\phi(t)$ is the stochastic bias instability term, which is modeled as if it is generated using a first-order Gauss–Markov

process as a shaping filter. The INS outputs for the pitch and yaw angles (θ and ψ) are also modeled to have similar error characteristics.

IV. Controller Design Based on Nonlinear Dynamic Inversion

In this study, the aerodynamic and thrust-vectoring controllers (based on NDI) are designed separately to command the aerodynamic control surfaces and the thrust-vectoring paddles. The thrust-vectoring controller is designed to be turned on whenever the aerodynamic controller loses its effectiveness due to excessive angle-of-attack values. Therefore, when the thrust vector controller is turned on, the aerodynamic controller is turned off and the aerodynamic surfaces are retracted to their neutral positions. In such a case, the aircraft is controlled only by using the thrust forces T_L and T_R generated by the two engines and the thrust vector deviation angle pairs (θ_L, θ_R) and (ψ_L, ψ_R).

The aim of the designed controller is to control the instantaneous attitude of the aircraft to perform the desired maneuvers at a high-α flight. To maneuver the aircraft as such, the yaw, pitch, and roll attitudes of the aircraft shall be controlled. Hence, the commanded control surface deflections $(\delta_{ac}, \delta_{ec}, \delta_{rc})$ for the aerodynamic control case and the commanded thrust vector deflections $(\theta_{Lc}, \theta_{Rc})$ and (ψ_{Lc}, ψ_{Rc}) for the thrust-vectoring control case shall be tied up to the desired yaw–pitch–roll attitudes of the aircraft. This is done in two steps, as described subsequently.

In the first step, the desired yaw, pitch, and roll attitudes of the aircraft are related to the commanded angular accelerations by using the slow-varying dynamic part of the two-time-scale separation scheme. In the second step, the commanded angular accelerations are related to the deflection angles of either the aerodynamic control surfaces or the TVC paddles by using the fast-varying dynamic part.

For the slow-varying dynamic part (i.e., for the attitude angles), the PI control law is used and named as the attitude controller. As for the fast-varying dynamic part (i.e., for the angular velocity components), the P control law is used and named as the angular velocity controller. Referring to the desired attitude angles $(\phi_d, \theta_d, \psi_d)$, the error vector $\bar{e}(t)$ is defined as the difference between the desired and the instantly measured attitude angles of the aircraft. Then, implementing a PI controller with constant gain matrices $\hat{K}_p = \text{diag}(K_{p\phi}, K_{p\theta}, K_{p\psi})$ and $\hat{K}_i = \text{diag}(K_{i\phi}, K_{i\theta}, K_{i\psi})$, the commanded rates of the roll, pitch, and yaw angles are calculated as follows:

$$\begin{bmatrix} \dot{\phi}_c(t) \\ \dot{\theta}_c(t) \\ \dot{\psi}_c(t) \end{bmatrix} = \hat{K}_p \bar{e}(t) + \hat{K}_i \int_0^t \bar{e}(t') \mathrm{d}t'$$

$$\bar{e}(t) = \begin{bmatrix} \phi_d(t) - \phi_m(t) \\ \theta_d(t) - \theta_m(t) \\ \psi_d(t) - \psi_m(t) \end{bmatrix} \quad (8)$$

Next, recalling the kinematic relationships between the angular velocity components and the derivatives of the attitude angles, the commanded values p_c, q_c, and r_c can be calculated from $\dot{\phi}_c$, $\dot{\theta}_c$, and $\dot{\psi}_c$ as shown next:

$$\begin{bmatrix} p_c \\ q_c \\ r_c \end{bmatrix} = \begin{bmatrix} 1 & 0 & -s\theta_m \\ 0 & c\phi_m & c\theta_m s\phi_m \\ 0 & -s\phi_m & c\theta_m c\phi_m \end{bmatrix} \begin{bmatrix} \dot{\phi}_c \\ \dot{\theta}_c \\ \dot{\psi}_c \end{bmatrix} \quad (9)$$

Afterward, $\bar{e}_r(t)$ is defined as the difference between the commanded and the measured values of the angular velocity components. Then, implementing a P controller with the gain matrix $\hat{K}_d = \text{diag}(K_{d\phi}, K_{d\theta}, K_{d\psi})$, the commanded angular accelerations $(\dot{p}_c, \dot{q}_c, \dot{r}_c)$ are calculated as follows:
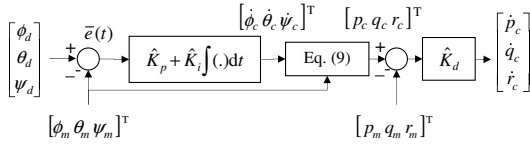
Fig. 5 Angular acceleration command generator.

$$\begin{bmatrix} \dot{p}_c(t) \\ \dot{q}_c(t) \\ \dot{r}_c(t) \end{bmatrix} = \hat{K}_d \bar{e}_r(t), \qquad \bar{e}_r(t) = \begin{bmatrix} p_c(t) - p_m(t) \\ q_c(t) - q_m(t) \\ r_c(t) - r_m(t) \end{bmatrix} \quad (10)$$

Equations (8–10) are represented as a block diagram, shown in Fig. 5.

If the aerodynamic control is to be used, the command values for the aerodynamic forces and moments can be calculated by using the dynamic inversion control law. Thus, for the commanded translational and angular accelerations and with undeflected TVC paddles, the following inverted equation can be written based on Eq. (4):

$$\begin{bmatrix} \bar{F}_{ac}^{(b)} \\ \bar{M}_{ac}^{(b)} \end{bmatrix} = \hat{H}^{-1} \left\{ \begin{bmatrix} [\dot{u}_c & \dot{v}_c & \dot{w}_c]^T \\ [\dot{p}_c & \dot{q}_c & \dot{r}_c]^T \end{bmatrix} - \bar{F} - \hat{G} \begin{bmatrix} [T_L & 0 & 0]^T \\ [T_R & 0 & 0]^T \end{bmatrix} \right\}$$

(11)

In Eq. (11), because there is not any particular control demand on the velocity vector, the command values of the translational accelerations ($\dot{u}_c, \dot{v}_c, \dot{w}_c$) are taken to be zero. Furthermore, the terms related to the angular momentum of the rotating engine parts are not taken into account. They are treated as unknown disturbance terms.

On the other hand, the aerodynamic moment components can be expressed as $M_{ax}^{(b)} = (Q_d Sb)C_l$, $M_{ay}^{(b)} = (Q_d S\bar{c})C_m$, and $M_{az}^{(b)} = (Q_d Sb)C_n$. Here, C_l, C_m, and C_n are the aerodynamic moment coefficients; Q_d is the dynamic pressure; S is the surface area of the wing planform; $\bar{c}$ is the mean chord length; and b is the span of the wings. C_l, C_m, and C_n can be related to the control surface deflections as

$$C_l = C_l'(\alpha, \beta, p, q, r) + C_{l\delta_a}(\alpha, \beta)\delta_a + C_{l\delta_r}(\alpha, \beta)\delta_r \quad (12a)$$

$$C_m = C_m'(\alpha, \beta, p, q, r) + C_{m\delta_e}(\alpha, \beta)\delta_e \quad (12b)$$

$$C_n = C_n'(\alpha, \beta, p, q, r) + C_{n\delta_a}(\alpha, \beta)\delta_a + C_{n\delta_r}(\alpha, \beta)\delta_r \quad (12c)$$

Hence, upon obtaining $\bar{M}_{ac}^{(b)}$ using Eqs. (11) and (12) gives the commanded aerodynamic control surface deflections as

$$\begin{bmatrix} \delta_{ac} \\ \delta_{ec} \\ \delta_{rc} \end{bmatrix} = \begin{bmatrix} C_{l\delta_a} & 0 & C_{l\delta_r} \\ 0 & C_{m\delta_e} & 0 \\ C_{n\delta_a} & 0 & C_{n\delta_r} \end{bmatrix}^{-1} \begin{bmatrix} M_{axc}^{(b)}/(Q_d Sb) - C_l' \\ M_{ayc}^{(b)}/(Q_d S\bar{c}) - C_m' \\ M_{azc}^{(b)}/(Q_d Sb) - C_n' \end{bmatrix} \quad (13)$$

If the thrust-vectoring control is to be used, the command values for the thrust forces, to be generated by the left and right engines, can again be calculated by using the dynamic inversion control law. In this case, for the commanded translational and angular accelerations and with undeflected aerodynamic control surfaces, the following equation can be written again based on Eq. (4):

$$\begin{bmatrix} \bar{F}_c^{(b)} \\ \bar{M}_c^{(b)} \end{bmatrix} = \hat{H}^{-1} \left\{ \begin{bmatrix} [\dot{u}_c & \dot{v}_c & \dot{w}_c]^T \\ [\dot{p}_c & \dot{q}_c & \dot{r}_c]^T \end{bmatrix} - \bar{F} - \hat{H} \begin{bmatrix} \bar{F}_a^{(b)} \\ \bar{M}_a^{(b)} \end{bmatrix} \right\} \quad (14a)$$

Here, the terms related to the angular momentum of the rotating engine parts are again not taken into account, because of the same reason mentioned earlier. On the other hand, it can be shown that

$$\begin{bmatrix} \bar{F}_c^{(b)} \\ \bar{M}_c^{(b)} \end{bmatrix} = \begin{bmatrix} \hat{I} & \hat{I} \\ \tilde{r}_{be_L}^{(b)} & \tilde{r}_{be_R}^{(b)} \end{bmatrix} \begin{bmatrix} \bar{F}_{Lc}^{(b)} \\ \bar{F}_{Rc}^{(b)} \end{bmatrix} \quad (14b)$$

Here, $\bar{F}_c^{(b)}$ and $\bar{M}_c^{(b)}$ are the necessary force and moment vectors to realize the commanded accelerations. Because the coefficient matrix in Eq. (14b) is rank-deficient, the consistency of this equation is satisfied by allowing freedom for certain components of $\bar{F}_c^{(b)}$ and $\bar{M}_c^{(b)}$ [41]. Defining the left and right engine nozzle exit locations by the position vectors $\bar{r}_{be_L}^{(b)} = [e_x \quad e_y \quad e_z]^T$ and $\bar{r}_{be_R}^{(b)} = [e_x \quad -e_y \quad e_z]^T$, the consistency of Eq. (14b) necessitates the following constraint equation:

$$M_{yc}^{(b)} = -e_x F_{zc}^{(b)} + e_z F_{xc}^{(b)} \quad (14c)$$

This equation, in turn, necessitates that only two of the three acceleration components ($\dot{u}, \dot{w}, \dot{q}$) can be commanded arbitrarily and the third one must obey the constraint dictated by Eq. (14c). In this study, $\dot{q}_c$ is already determined by Eq. (10) as a result of the required angular maneuver, and $\dot{u}_c$ and $\dot{v}_c$ are taken to be zero, as mentioned following Eq. (11). Consequently, $\dot{w}_c$ is calculated depending on these values of $\dot{q}_c$ and $\dot{u}_c$. Then the control allocation between the left and right engine command values for the thrust forces $\bar{F}_{Lc}^{(b)}$ and $\bar{F}_{Rc}^{(b)}$ are calculated by using the table of achievable desired forces and moments given in [41]. Afterward, their spherical components $\{T_{Lc}, \psi_{Lc}, \theta_{Lc}\}$ and $\{T_{Rc}, \psi_{Rc}, \theta_{Rc}\}$ can be determined. Then, using T_{Lc} and T_{Rc} and taking $P_{a_{Lc}} = P_{c_{Lc}}$ and $P_{a_{Rc}} = P_{c_{Rc}}$, the throttle positions δ_{thLc} and δ_{thRc} can be found from Eqs. (6) and (7). As for the six thrust-vectoring paddle deflections ($\delta_{Lc(1,2,3)}, \delta_{Rc(1,2,3)}$), they are determined by using the transformation between them and the commanded thrust deviation angles, as explained in [41].

The aerodynamic controls can effectively be used in flight regimes with low to moderate angles of attack. However, they are ineffective in flight regimes with high angles of attack. Hence, at stall/poststall conditions, it is beneficial to use the thrust-vectoring control. So, for challenging flight maneuvers, the aerodynamic and thrust-vectoring controls are used together. The blending strategy is basically dependent on the saturation of the aerodynamic control surfaces ($\delta_e, \delta_a, \delta_r$). They are monitored together with the estimated values of $C_{n\beta dyn}$ and LCDP continuously and checked whether they are saturated and/or the stall indication parameters are negative. For example, whenever the ailerons saturate, they are commanded to their neutral positions; thereafter, the roll motion of the desired maneuver is achieved by TVC until the aerodynamic control algorithm yields an unsaturated aileron command again. The same is also true for the rudder and elevator surfaces. If $C_{n\beta dyn}$ and LCDP indicate that the aircraft is in a stall-safe region, as depicted in Fig. 4, then the elevators are commanded to their trim positions corresponding to that instant of the flight. Based on the preceding discussion about switching between the aerodynamic and thrust-vectoring controls, the NDI block diagram that describes the process initiated by the commanded angular accelerations is shown in Fig. 6.

Assuming that there are no uncertainties and no saturations due to the limitations on the control effectors, the NDI approach produces a linear system of three independent and decoupled free integrators between the $\dot{p}_c$, $\dot{q}_c$, and $\dot{r}_c$ and the ϕ_m, θ_m, and ψ_m channels. This is shown with the angular acceleration command generator in Fig. 7.

Hence, considering the attitude and the angular velocity controller together, the ideal closed-loop transfer functions can be written as follows:
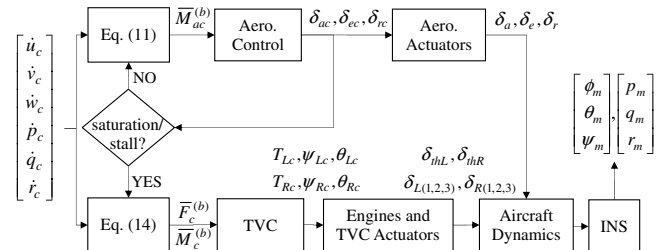
Fig. 6 NDI block diagram for angular accelerations with aerodynamic and thrust-vectoring controls.
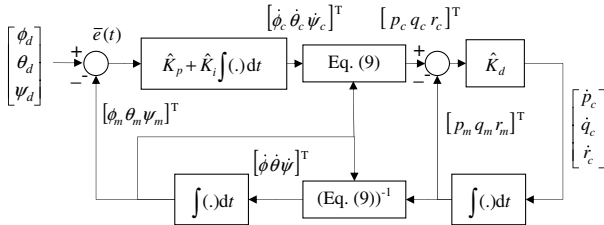
Fig. 7   Block diagram of the ideally inverted and controlled system.

Fig. 8   Compact representation of the inverted nonlinear dynamics.

$$\frac{\phi_m(s)}{\phi_d(s)} = \frac{K_{d\phi}(K_{p\phi}s + K_{i\phi})}{s^3 + K_{d\phi}s^2 + K_{p\phi}K_{d\phi}s + K_{i\phi}K_{d\phi}}$$

$$\frac{\theta_m(s)}{\theta_d(s)} = \frac{K_{d\theta}(K_{p\theta}s + K_{i\theta})}{s^3 + K_{d\theta}s^2 + K_{p\theta}K_{d\theta}s + K_{i\theta}K_{d\theta}}$$

$$\frac{\psi_m(s)}{\psi_d(s)} = \frac{K_{d\psi}(K_{p\psi}s + K_{i\psi})}{s^3 + K_{d\psi}s^2 + K_{p\psi}K_{d\psi}s + K_{i\psi}K_{d\psi}}$$

To calculate the diagonal gain matrices $\hat{K}_p$, $\hat{K}_i$, and $\hat{K}_d$, the poles of the desired closed-loop dynamics of the attitude angles should be specified. Here, these poles are specified as three sets, in which each one consists of a complex conjugate pole pair and a real pole, as shown next:

$$\{-\omega_{n\phi}(\zeta_\phi \pm j(1 - \zeta_\phi^2)^{1/2}), -\omega'_{n\phi}\}, \{-\omega_{n\theta}(\zeta_\theta \pm j(1 - \zeta_\theta^2)^{1/2}), -\omega'_{n\theta}\}$$

$$\{-\omega_{n\psi}(\zeta_\psi \pm j(1 - \zeta_\psi^2)^{1/2}), -\omega'_{n\psi}\}$$

The calculation of the controller gain matrices corresponding to the preceding poles selected is explained in [41]. The poles of the desired closed-loop dynamics for the attitude control must be selected considering the desired agility and the robust performance of the aircraft.

V.   Robust Performance Analysis

In the previous section, it is mentioned that without the plant uncertainties, disturbances, and saturations, the NDI method described in Fig. 6 will produce a linear system of three independent and decoupled free integrators (i.e., a perfectly inverted system). However, when disturbances and modeling uncertainties exist, the inverted system will deviate from the ideally inverted system. Hence, by linearizing the inversion loop with ideal NDI [i.e., Eqs. (11) and (14)], but by adding the modeling uncertainties in the aircraft dynamics, the resultant perturbed system can be obtained. Furthermore, by subtracting the ideal system equations from those of the perturbed system, the uncertainties can be represented as linear additive uncertainties. Thus, any robust performance analysis method using linear system matrices can be applied on the perturbed system. Motivated by this idea, the robust performance analysis is carried out by linearizing the system depicted in Fig. 6 at a representative flight condition and applying the structured singular-value μ analysis.

For the purpose of robustness analysis, first, the trim values of the total thrust force T_0, the angle of attack α_0, the sideslip angle β_0, and the aerodynamic control surfaces ($\delta_{a0}, \delta_{e0}, \delta_{r0}$) are calculated by solving the Newton–Euler equations, given in Eq. (2), at the desired altitude h_0, Mach number M_0, and (ϕ_0, θ_0). Throughout the calculations, due to the nonlinearity of the Newton–Euler equations, it is possible to obtain multiple solutions. Hence, the trimming results are chosen as the physically realizable ones of the multiply calculated values of δ_{a0}, δ_{e0}, δ_{r0}, α_0, and T_0. In other words, if the calculated aerodynamic control surface deflections are not within the saturation limits, the total thrust is not within the capabilities of the engine and the angle of attack is not within the region for which the aerodynamic coefficients are associated with, then they are not counted as the feasible solutions of the trimming algorithm. Applying the trimming algorithm as mentioned, the trim points are calculated for
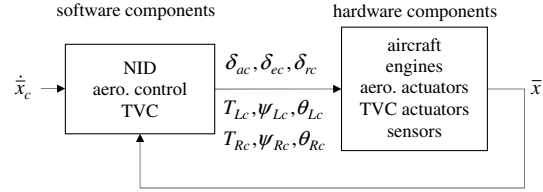
$$0 \text{ m} \leq h_0 \leq 15,000 \text{ m}, \quad 0.1 \leq M_0 \leq 1.5, \quad \text{and} \quad \phi_0 = \theta_0 = p_0 = q_0 = r_0 = 0.$$

After the determination of the trim points, the system depicted in Fig. 6 is linearized around these points. Note that the controlled system consists of two main parts, as shown in Fig. 8. The first part is composed of the control software components: that is, the NID algorithm as expressed by Eqs. (11) and (14), the aerodynamic control algorithm, and the thrust-vectoring control algorithm. The second part is composed of the plant (aircraft), the engines, the actuators, and the sensors. In Fig. 8, $\bar{x} = [u \quad v \quad w \quad p \quad q \quad r]^T$ and $\dot{\bar{x}}_c = [\dot{u}_c \quad \dot{v}_c \quad \dot{w}_c \quad \dot{p}_c \quad \dot{q}_c \quad \dot{r}_c]^T$.

Referring to Fig. 8, two sets of transfer matrices can be calculated. The first set can be calculated by linearizing the system with the nominal parameters of the hardware and software components that are in common. As for the second set, the common parameters can be kept nominal in the software components, but they can be perturbed in the hardware components. By subtracting the system matrices of the perturbed system (i.e., the second set) from those of the nominal system (i.e., the first set), the additive uncertainties associated with the ideally inverted system (with nominal plant parameters) can be calculated. The details are explained subsequently.

The nonlinear system in Fig. 8 can be represented by a nonlinear function as $\dot{\bar{x}} = \bar{f}(\bar{x}, \dot{\bar{x}}_c)$. Hence, linearizing the system depicted in Fig. 8 around the desired flight condition and the calculated trim points (i.e., $\bar{x}_0 = [u_0 \quad v_0 \quad w_0 \quad p_0 \quad q_0 \quad r_0]^T$ and $\dot{\bar{x}}_{c0} = [\dot{u}_{c0} \quad \dot{v}_{c0} \quad \dot{w}_{c0} \quad \dot{p}_{c0} \quad \dot{q}_{c0} \quad \dot{r}_{c0}]^T$), the following state-space representation is obtained:

$$\Delta\dot{\bar{x}} = \hat{A}\Delta\bar{x} + \hat{B}\Delta\dot{\bar{x}}_c$$

where

$$\hat{A} = \frac{\partial \bar{f}}{\partial \bar{x}}\bigg|_{\bar{x}_0, \dot{\bar{x}}_{c0}}, \qquad \hat{B} = \frac{\partial \bar{f}}{\partial \dot{\bar{x}}_c}\bigg|_{\bar{x}_0, \dot{\bar{x}}_{c0}}$$

The linearized dynamics described by the preceding equations can be expressed in the Laplace domain as $\Delta\bar{X}(s) = \hat{G}_{\text{nom}}(s)\Delta\dot{\bar{X}}_c(s)$, where the transfer matrix $\hat{G}_{\text{nom}}(s)$ is defined as follows:

$$\hat{G}_{\text{nom}}(s) = (s\hat{I} - \hat{A})^{-1}\hat{B} = $$

$$\begin{bmatrix} \begin{bmatrix} G_{u\dot{u}}(s) & 0 & G_{u\dot{w}}(s) \\ 0 & G_{v\dot{v}}(s) & 0 \\ 0 & 0 & 0 \end{bmatrix} & \hat{0}_{3\times3} \\ \begin{bmatrix} 0 & 0 & 0 \\ 0 & 0 & G_{q\dot{w}}(s) \\ 0 & 0 & 0 \end{bmatrix} & \begin{bmatrix} G_{p\dot{p}}(s) & 0 & 0 \\ 0 & G_{q\dot{q}}(s) & 0 \\ 0 & 0 & G_{r\dot{r}}(s) \end{bmatrix} \end{bmatrix}$$

(15)

Looking at the expression of $\hat{G}_{\text{nom}}(s)$, it is seen that the linearization produces cross-coupling transfer functions $G_{uw}(s)$ and $G_{qw}(s)$ that relate $\Delta\dot{w}_c$ to Δu and Δq. Moreover, Δw is not excited by any of the commanded acceleration inputs. This is a consequence of the constraint equation for u, w, and q [i.e., Eq. (14c)], mentioned in Sec. IV.

As an example, the results of the trimming algorithm and the linearization are presented subsequently for a representative flight condition at $h_0 = 7500$ m and $M_0 = 0.95$ with $T_0 = 26,428$ N, $\alpha_0 = 0.33$ deg, $\delta_{e0} = -1.14$ deg, and $\beta_0 = \delta_{a0} = \delta_{r0} = 0$. At this flight condition, the elements of the transfer matrix $\hat{G}_{\text{nom}}(s)$ are found as follows:

$$G_{u\dot{u}}(s) = G_{v\dot{v}}(s) = G_{w\dot{w}}(s) = G_{p\dot{p}}(s) = G_{r\dot{r}}(s) = \frac{1}{s}$$

$$G_{u\dot{w}}(s) = \frac{-0.14}{s(s+0.69)}, \qquad G_{q\dot{w}}(s) = \frac{1.40s + 295}{s(s+0.69)} \qquad (16)$$

Because the additive uncertainties associated with the ideally inverted system are generated by using the mentioned trimming and the linearization algorithms together, their success is tested by simultaneous simulations of the linearized system represented by $\hat{G}_{\text{nom}}(s)$ and the nonlinear system. The simulations are carried out with $\dot{u}_c = \dot{v}_c = 0$ and nonzero $\dot{p}_c$, $\dot{q}_c$, and $\dot{r}_c$, which are chosen as zero mean white noise signals with Gaussian distribution and with standard deviation values of $\sigma_{\dot{p}} = \sigma_{\dot{q}} = \sigma_{\dot{r}} = 100 \deg/s$. Note that w is not effectible by the commanded accelerations according to Eq. (15) when the proposed TVC is used. Therefore, in the simulations, $\dot{w}_c$ is not specified, but it is calculated using the specified values of $\dot{q}_c$ and $\dot{u}_c$ according to Eq. (14c). Thus, w is left to change freely. During the simulations, for the same specified nonzero inputs $(\dot{p}_c, \dot{q}_c, \dot{r}_c)$, the outputs (p, q, r) of the linearized system with $\hat{G}_{\text{nom}}(s)$ and the nonlinear system are compared. The results plotted in Fig. 9 show that the outputs of the two systems match each other almost perfectly. Hence, this demonstrated success of the trimming and linearization approach shows that the additive uncertainties associated with the ideally inverted system can be calculated by the proposed method explained in the previous paragraphs.

A.   Uncertainty Estimation for Robust Performance Analysis

For a proper application of the NDI method, it is very crucial to identify the parameters and model the dynamics of the nonlinear plant exactly. In most of the flight control problems, the important parameters are the aerodynamic coefficients. They are conventionally estimated by using the databases (aided by semi-empirical methods) of similar air vehicles, wind-tunnel tests, computational fluid dynamics (CFD), and flight tests. All of these methods have certain estimation errors dependent on several factors. That is, the

technique and methodology of estimation, the flight conditions at which the estimations are made, and the geometry of the aircraft are very important factors affecting the estimation accuracy. The estimation errors on the aerodynamic coefficients are generally specified with percentages. Figure 10 shows an example for comparison of some aerodynamic coefficient derivatives estimated by using the Kay vortex-lattice method, which is a CFD method based on vortex ring assignment [46], and the U.S. Air Force digital DATCOM [47] for an F-18-type configuration. The deviations of the aerodynamic coefficient derivatives calculated with these methods from their nominal values [i.e., data (as denoted in Fig. 10)] are different and their differences are dependent on the flight conditions.

Recall that, as explained in Sec. III, the commanded forces and moments ($\bar{F}_c^{(b)}$ and $\bar{M}_c^{(b)}$) are calculated by using the aerodynamic forces and moments ($\bar{F}_a$ and $\bar{M}_a$), which are functions of the aerodynamic coefficients. Hence, the estimation errors of the aerodynamic coefficients will directly affect $\bar{F}_c^{(b)}$ and $\bar{M}_c^{(b)}$ and, consequently, $\bar{F}_{Lc}^{(b)}$ and $\bar{F}_{Rc}^{(b)}$. Eventually, the estimation errors of the aerodynamic coefficients will directly affect the control surface commands and degrade the performance of the designed controller or even cause an improper operation. Therefore, it is crucial to analyze the effects of the aerodynamic coefficient uncertainties on the controller performance.

The uncertainty definition starts with a very challenging assumption: suppose that the aerodynamic coefficients are completely unknown and cannot be included within the NID process. This means that the effect of the aerodynamics is ignored in the nonlinear dynamic inversion (i.e., $\bar{F}_a = \bar{M}_a = \bar{0}$ in the software components block, as depicted in Fig. 8). In other words, the uncertainty in the aerodynamic coefficients of the aircraft to be controlled is 100%. This idea is taken into consideration to eliminate the lengthy and costly high-α aerodynamic analyses, which may be considered unnecessary, whereas TVC is already available to achieve the required maneuvers. Hence, the entire control action is desired to be realized only by the TVC with the additional purpose of suppressing the disturbance coming from the total aerodynamics of the aircraft.

The linearization of the NID (without aerodynamic terms) together with the aircraft dynamics (including the aerodynamic effects) lead to the perturbed transfer matrix $\hat{G}(s)$, and the difference between the perturbed and nominal transfer matrices [i.e., $\Delta\hat{G}(s) = \hat{G}(s) - \hat{G}_{\text{nom}}(s)$] is assigned as the additive uncertainty matrix on the nominal transfer matrix. The detailed expression of the difference matrix is shown next:
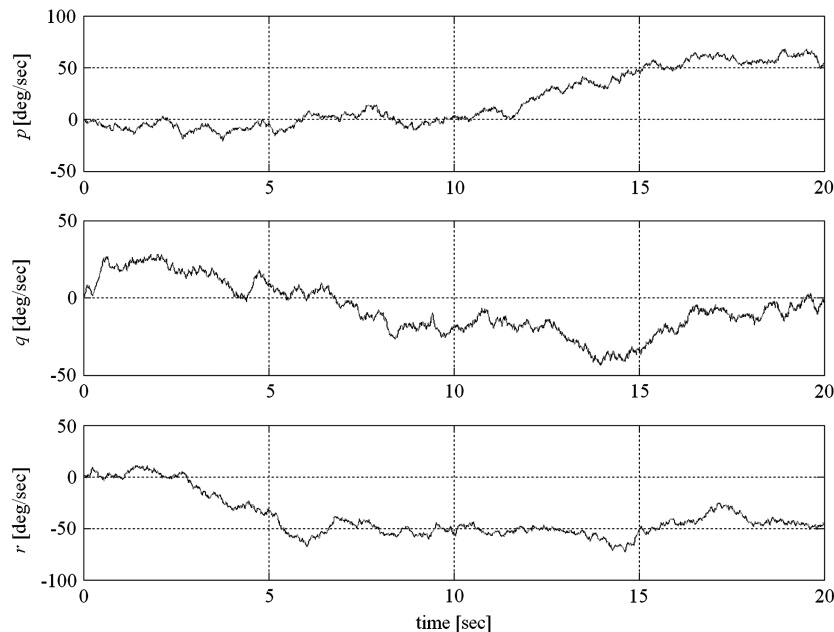

**Fig. 9   Angular velocity outputs of the systems with nonlinear and linearized dynamics.**
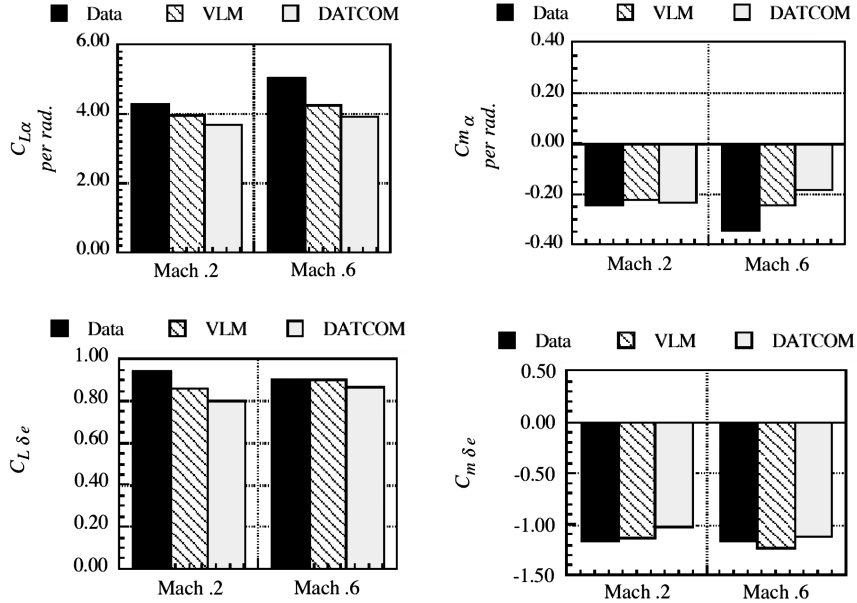
Fig. 10   Uncertainties in the aerodynamic coefficients for an F-18 aircraft [46].

$$\Delta\hat{G}(s) = \begin{bmatrix} \begin{bmatrix} & \hat{0}_{3\times 3} & \\ 0 & \Delta G_{v\dot{p}}(s) & 0 \\ \Delta G_{u\dot{q}}(s) & 0 & \Delta G_{w\dot{q}}(s) \\ 0 & \Delta G_{v\dot{r}}(s) & 0 \end{bmatrix} & \begin{bmatrix} & \hat{0}_{3\times 3} & \\ \Delta G_{p\dot{p}}(s) & 0 & 0 \\ 0 & \Delta G_{q\dot{q}}(s) & 0 \\ 0 & 0 & \Delta G_{r\dot{r}}(s) \end{bmatrix} \end{bmatrix} \tag{17}$$

Hence, at the same representative flight condition mentioned previously, the elements of $\Delta\hat{G}(s)$ are found as

$$\Delta G_{v\dot{p}}(s) = \frac{0.30s + 0.21}{s^2(s + 0.79)}, \qquad \Delta G_{p\dot{p}}(s) = \frac{2s^2 + 1.59s + 0.15}{s^2(s + 0.79)}$$

$$\Delta G_{u\dot{q}}(s) = \frac{s(-0.28s - 0.22)}{s^2(s + 0.79)}$$

$$\Delta G_{w\dot{q}}(s) = \frac{3.33s^2 + 589.78s + 62.91}{s^2(s + 0.79)}$$

$$\Delta G_{q\dot{q}}(s) = \frac{2s^2 + 1.59s + 0.15}{s^2(s + 0.79)}, \qquad \Delta G_{v\dot{r}}(s) = \frac{s(-1.58s - 1.08)}{s^2(s + 0.79)}$$

$$\Delta G_{r\dot{r}}(s) = \frac{2s^2 + 1.59s + 0.15}{s^2(s + 0.79)}$$

The block diagram of the linearized nonlinear dynamics with $\hat{G}_{nom}(s)$ and the additive uncertainty transfer matrix $\Delta\hat{G}(s)$ is shown in Fig. 11.

B.   Robust Performance Analysis of the Designed Controller

The designed controller is composed of the attitude and the angular velocity controllers. They are constructed by using the PI and P controller structures with the gain matrices $\hat{K}_p$, $\hat{K}_i$, and $\hat{K}_d$, as shown in Fig. 5. In the robust performance analysis, to make the analysis under the effect of maximum noise contribution, the shaping
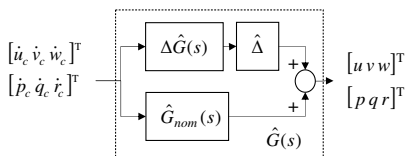
Fig. 11   Representation of additive uncertainty $\Delta\hat{G}(s)$ on $\hat{G}_{nom}(s)$.

filters of the measurement noise signals are set to unity so that $n_\phi = w_\phi$, $n_\theta = w_\theta$, $n_\psi = w_\psi$, $n_p = w_p$, $n_q = w_q$, and $n_r = w_r$.

The performance of the designed controller is examined by comparing the output of the controlled system with the output corresponding to the desired closed-loop dynamics [i.e., the desired matching model $\hat{G}_{des}(s)$]. The difference between the outputs of the desired matching model and the controlled model are processed with the performance weight transfer matrix $\hat{W}_p(s)$, and the structured singular values μ are calculated with respect to the outputs of the block with $\hat{W}_p(s)$ (i.e., $\delta\phi$, $\delta\theta$, and $\delta\psi$). The angular acceleration command generator, the desired matching model, and the performance weight transfer matrix with the noise signals $(n_\phi, n_\theta, n_\psi, n_p, n_q, n_r)$ and the sensor biases $(b_\phi, b_\theta, b_\psi, b_p, b_q, b_r)$ are shown in the block diagram in Fig. 12.

Recall that in Sec. III, the poles of the desired closed-loop dynamics are specified in terms of the parameter sets $\{\omega_{n\phi}, \omega_{n\theta}, \omega_{n\psi}\}$, $\{\omega'_{n\phi}, \omega'_{n\theta}, \omega'_{n\psi}\}$, and $\{\zeta_\phi, \zeta_\theta, \zeta_\psi\}$. Considering the robust stability and the nominal performance characteristics under the effect of the described plant uncertainties and external disturbances, they are set to $\omega_{n\phi} = \omega_{n\theta} = \omega_{n\psi} = 1$ Hz, $\omega'_{n\phi} = \omega'_{n\theta} = \omega'_{n\psi} = 7$ Hz, and $\zeta_\phi = \zeta_\theta = \zeta_\psi = 1$ after successive trials and errors. Here, the aim of the trial-and-error study is to choose the controller parameters and design a controller capable of making the desired maneuvers in a satisfactory manner. Then, using these values, the desired matching model and the performance weighting transfer matrices are formed as follows:

$$\hat{G}_{des}(s) = \text{diag}\left(\frac{\omega_{n\phi}}{s + \omega_{n\phi}}, \frac{\omega_{n\theta}}{s + \omega_{n\theta}}, \frac{\omega_{n\psi}}{s + \omega_{n\psi}}\right) \tag{18a}$$

$$\hat{W}_p(s) = \text{diag}\left(\frac{s + 30\omega_{n\phi}}{10(s + 3\omega_{n\phi})}, \frac{s + 30\omega_{n\theta}}{10(s + 3\omega_{n\theta})}, \frac{s + 30\omega_{n\psi}}{10(s + 3\omega_{n\psi})}\right) \tag{18b}$$

Here, the elements of the desired matching model $\hat{G}_{des}(s)$ are set in the form of low-pass filters with the cutoff frequencies at $\omega_{n\phi}$, $\omega_{n\theta}$,
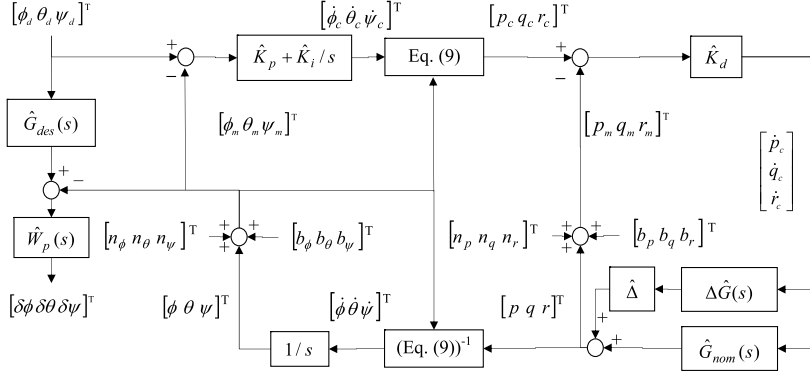
Fig. 12   Block diagram for robust performance analysis.

and $\omega_{n\psi}$, which are the magnitudes of the dominant closed-loop poles of the inverted and controlled nonlinear system. On the other hand, the elements of the performance weight transfer matrix $\hat{W}_p(s)$ are chosen in the form of lead-lag filters that suppress the effects of the inputs with frequencies higher than the bandwidth frequencies of the desired matching model and the proposed attitude control system. The Bode plot of each element of the performance weight transfer matrix turns out to be as shown in Fig. 13 for $\omega_{n\phi} = \omega_{n\theta} = \omega_{n\psi} = 2\pi$ rad/s.
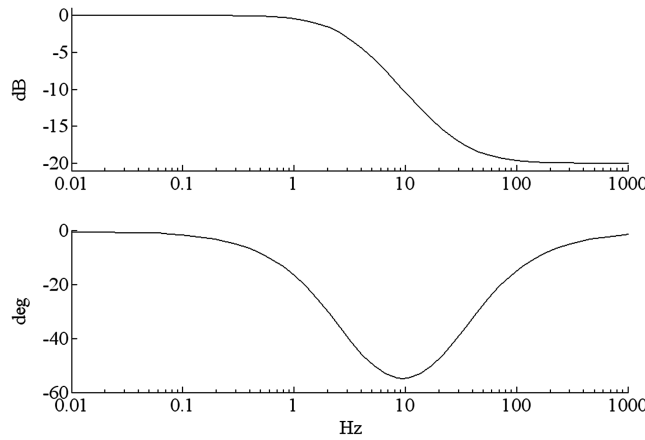
Fig. 13   Common Bode plot of the elements of the performance weight transfer matrix.

Using the given controller parameter set, the graphs that show the frequency variations of μ, the robust stability, and the nominal performance are drawn in Fig. 14 for $\bar{F}_a = \bar{M}_a = \bar{0}$. As shown in Fig. 14, the peak value of μ happens to be 3.21, which implies that $\|\hat{F}_u(\hat{M}, \hat{\Delta})\|_\infty \leq 3.21$.

Hence, with the specified controller parameters, it is concluded that the controlled system is only robust to the $1/3.21$ of the specified external disturbances and uncertainties. This analysis shows clearly that the robust performance cannot be achieved for the controller designed with the assumption that $\bar{F}_a = \bar{M}_a = \bar{0}$.

Based on the conclusion obtained previously, instead of totally ignoring the aerodynamic forces and moments, they should be included in the dynamic inversion process with a certain amount of accuracy. Hence, the aerodynamic forces are included in the NID process, but the uncertainties in the aerodynamic coefficients in the plant model are set to a level of 30%; that is, the aerodynamic coefficients are assumed to be 70% accurate. At this point, it must be pointed out that 30% uncertainty is relatively high when the general accuracy of the estimation methods is considered. In the analysis, all of the aerodynamic coefficients, except the drag coefficient C_x, are decreased to 70% of their nominal values. Thus, the lifting and maneuvering capabilities of the aircraft are degraded. However, the drag coefficient is increased to 130% of its nominal value to degrade the performance of the aircraft even further. For this case, the frequency variations of μ, the robust stability, and the nominal performance are drawn in Fig. 15. As seen in Fig. 15, the peak value of μ reaches only 0.92 this time [i.e., $\|\hat{F}_u(\hat{M}, \hat{\Delta})\|_\infty \leq 0.92$]. This result shows that a robust performance can be achieved if the
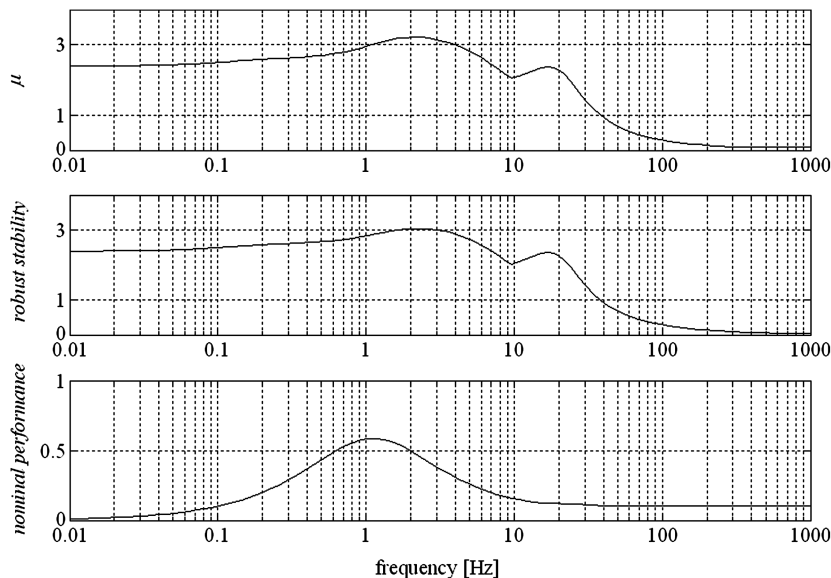

Fig. 14   Robust performance plots for the controller designed with $\bar{F}_a = \bar{M}_a = \bar{0}$.
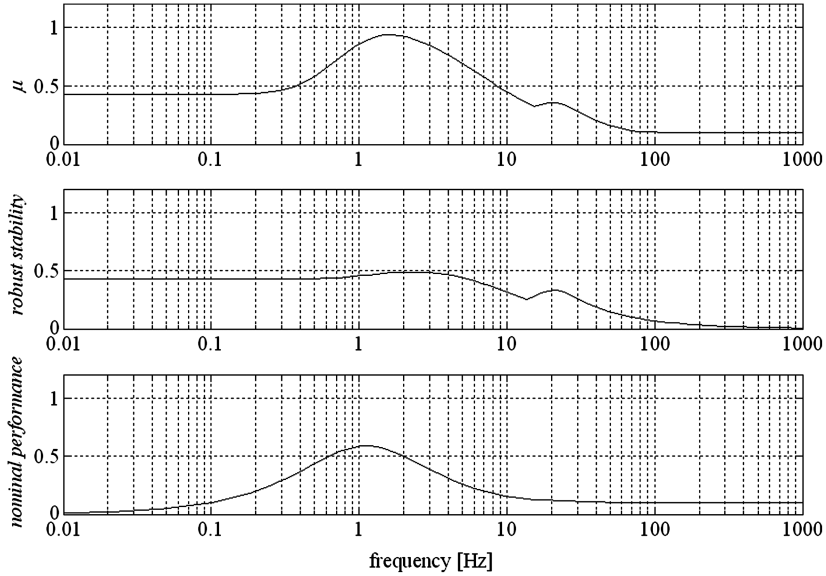
Fig. 15 Robust performance plots for the controller subjected to 70% uncertainty of $\bar{F}_a$ and $\bar{M}_a$.
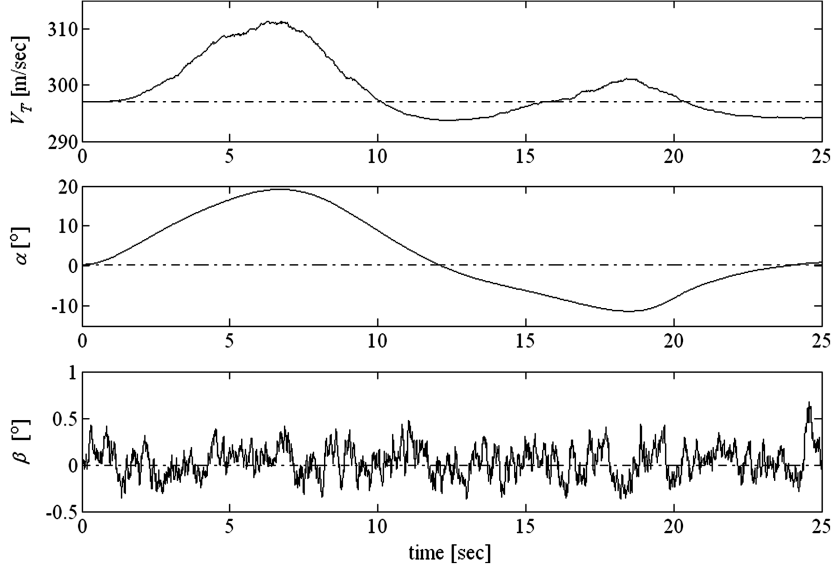
Fig. 16 V_T, α, and β plots with 30% uncertainty in the aerodynamic coefficients.

controller is designed with even 30% uncertainty in the estimation of the aerodynamic coefficients.

VI. Simulation and Verification of the Designed Controller

The robust performance analysis results of the previous section are verified here by simulating the flight of the aircraft under the action of the designed controller. The simulation is carried out by using the control parameters mentioned in the previous section and assuming that the aerodynamic coefficients have 30% uncertainty. The reference inputs for the translational accelerations are chosen as $\dot{u} = \dot{v} = \dot{V}_T = \dot{\beta} = 0$.

In the simulation, the attitude angle commands of the selected test maneuver are generated to achieve rapid pull-ups and turns. That is, the aircraft is commanded to pull up to 85 deg from 0 deg pitch angle and to make a full heading reversal at the same time. At the end of the maneuver, it is commanded to recover the level position again and simultaneously to complete a 180 deg heading change. The time to complete the maneuver is set as 20 s. For this maneuver, the reference attitude commands for the pitch and yaw motions are generated as

half-cycloid motions with $\theta_{max} = 85$ deg, $\psi_{final} = 180$ deg, and $t_{max} = 20$ s; that is,

$$\theta_d(t) = (\theta_{max}/2)(1 - \cos(2\pi(t/t_{max})))$$

$$\psi_d(t) = \psi_{final}((t/t_{max}) - (1/2\pi)\sin(2\pi(t/t_{max}))) \qquad (19)$$

As for the reference roll command, it is specified as follows in connection with the yaw command:

$$\phi_d(t) = k'\tan^{-1}\left(\frac{g}{V_T\dot{\psi}_d(t)}\right), \qquad k' = 0.6 \qquad (20)$$

Here, k' is chosen to coordinate the roll command suitably with the desired turn rate command. In the simulation, the standard deviations of the sensor measurement noises are chosen as $\sigma_\phi = \sigma_\theta = 0.3$ deg, $\sigma_\psi = 0.1$ deg, $\sigma_p = \sigma_q = \sigma_r = 1$ deg/h, and $\sigma_{\dot{u}} = \sigma_{\dot{v}} = 1$ m/s^2. The simulation results are plotted as shown in Figs. 16–18. In the plots, the dashed–dotted lines show the reference inputs and the continuous lines show the responses. Note that the reference and response signals in Fig. 18 are almost the same.
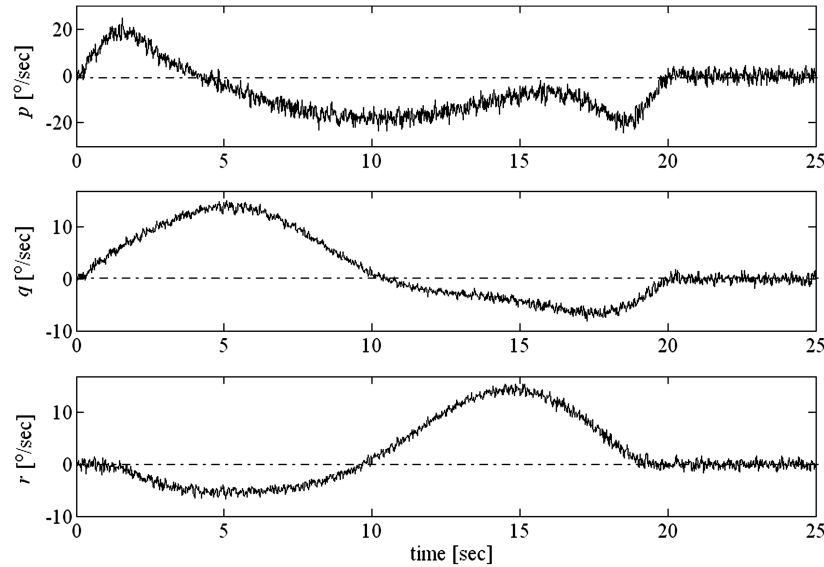
Fig. 17 Plots of *p*, *q*, and *r* with 30% uncertainty in the aerodynamic coefficients.
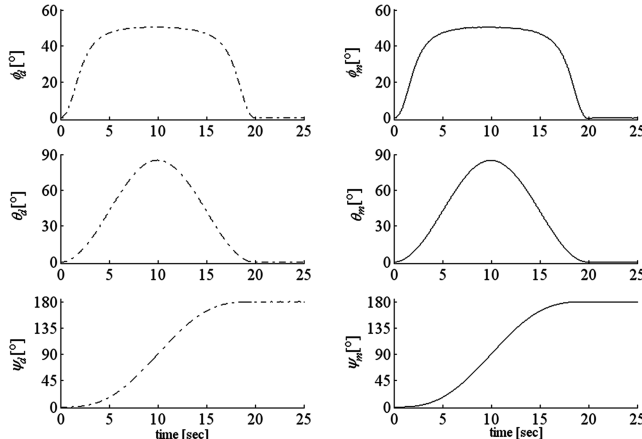
Fig. 18 Plots of ϕ, θ, and ψ with 30% uncertainty in the aerodynamic coefficients.

VII. Conclusions

In this study, an attitude control structure based on nonlinear dynamic inversion (NDI) is proposed and applied on a fighter aircraft model. The controller is designed to achieve automated agile maneuvers at high angles of attack with aerodynamic control if possible and with thrust-vectoring control otherwise. For this purpose, the maneuverability of the modeled aircraft is enhanced by integrating virtual thrust-vectoring postexit vanes to the nozzle exits of each engine. Then the robust performance of the designed controller is investigated under the effect of the sensor noise and aerodynamic uncertainties. Because NDI leads to similar performance at every flight condition and the additive uncertainty transfer functions turn out to be very close to each other over the whole flight envelope, the results of the robustness analysis pursued at a single representative flight condition are considered to be sufficient.

The uncertainties in the aerodynamic coefficients generally increase and become more unpredictable with the increasing angle-of-attack values. In this study, this fact is not taken into account in the robustness analysis and the aerodynamic uncertainties are assumed to be the same at every angle-of-attack value throughout the challenging flight conditions that can be coped with only by using TVC. However, the robustness analysis for TVC is repeated for two distinct cases. In the first case, a very extreme assumption is made and the aerodynamic forces and moments are treated as if they are completely unknown, and so they are modeled to be zero. The results of the robustness analysis clearly show that it is impossible to achieve

the desired performance with this assumption. In the second case, the aerodynamic forces and moments are assumed to be known but still with a large degree of uncertainty, such as 30%. In other words, to be on the worst side, the drag coefficient is assumed to be 30% larger than its nominal value, with the other coefficients 30% smaller than their nominal values. In this case, the results of the robustness analysis show that it is possible to design a TVC that can perform satisfactorily. Hence, it is concluded that even a rough estimation of the aerodynamic forces and moments with a certain minimum level of confidence makes it possible to design a robust TVC.

This study has also shown that high-angle-of-attack maneuvers can be automated by means of a TVC designed by using the proposed NDI approach. In fact, the performance of the designed TVC is demonstrated by simulating a difficult test maneuver that can be used in an actual air-to-air combat.

As for the future work, the stability and robustness of the proposed controller can be analyzed by implementing nonlinear analysis tools to account for the changing dynamic behavior of the aircraft over the whole maneuvering envelope. Furthermore, the switching between the aerodynamic and thrust-vectoring controls can be studied to propose different blending rules that optimize the full control authority and allow smooth transitions. In this paper, the plant uncertainty is accounted only in the aerodynamic forces and moments. However, it is also possible to consider uncertainties in different plant parameters such as aircraft mass/inertia, engine thrust, actuator/sensor dynamics, etc. On the other hand, it is also possible to enhance the flight scenarios and test the proposed controller further. The enhanced flight scenarios, which demonstrate high-angle-of-attack maneuvering superiority, can be selected as the well-known Cobra and Herbst, velocity vector roll, ground target attack, tail chaise acquisition, and target aircraft pointing maneuvers.

Another point is that the test maneuver simulated in this paper is assumed to be performed in an automated manner. However, it is also possible to extend this study to the pilot in the loop maneuvers. Such a study requires the integration of a human-pilot model into the controller design and the robust performance analysis. Thus, it may become possible to develop control structures that may ease the pilot workload during the severe maneuvers.

References

[1] Mason, W. H., "High Angle of Attack Aerodynamics," Aerospace and Ocean Engineering, Virginia Polytechnic Inst. and State Univ., Rept. AOE 4124, Blacksburg, VA, Mar. 2006, http://www.aoe.vt.edu/~mason/Mason_f/ConfigAeroHiAlphaNotes.pdf [retrieved May 2009].
[2] Pachter, M., and Chandler, P. R., "Velocity Vector Roll Control," AIAA Guidance, Navigation, and Control Conference, San Diego, CA, AIAA

Paper 96-3867, July 1996.

[3] Pachter, M., Chandler, P. R., and Smith, L., "Maneuvering Flight Control," *Journal of Guidance, Control, and Dynamics*, Vol. 21, No. 3, May–June 1998, pp. 368–374.
doi:10.2514/2.4264

[4] Murayama, K., and Hull, D. G., "The Cobra Maneuver as a Minimum Time Problem," AIAA Guidance, Navigation, and Control Conference, AIAA Paper 97-3586.

[5] Komduur, H. J., and Visser, H. G., "Optimization of Vertical Plane Cobra-Like Pitch Reversal Maneuvers," AIAA Atmospheric Flight Mechanics Conference and Exhibit, Montreal, Canada, AIAA Paper 2001-4134, Aug. 2001.

[6] Herbst, W. B., and Krogull, B., "Design for Air Combat," 4th AIAA Aircraft Design, Flight Test, and Operations Meeting, Los Angeles, AIAA Paper 1972-749, Aug. 1972.

[7] Herbst, W. B., "Dynamics of Air Combat," *Journal of Aircraft*, Vol. 20, No. 7, 1983, pp. 594–598.
doi:10.2514/3.44916

[8] Herbst, W. B., "Future Fighter Technologies," *Journal of Aircraft*, Vol. 17, No. 8, 1980, pp. 561–566.
doi:10.2514/3.44674

[9] Herbst, W. B., "X-31A at First Flight," *Flying Qualities*, AGARD CP-508, Neuilly sur-Seine, France, Feb. 1991, pp. 29-1–29-8.

[10] Canter, D. E., "X-31 Post-Stall Envelope Expansion and Tactical Utility Testing," *Fourth High Alpha Conference*, Vol. 2, NASA CP-10143, July 1994.

[11] Kidman, D. S., Vickers, J. E., Olson, B. P., and Gerzanics, M. A., "Evaluation of the F-16 Multi-Axis Thrust Vectoring Aircraft," U.S. Air Force Flight Test Center TR-95-12, Edwards AFB, CA, Sept. 1995.

[12] Smith, W., "X-29 High AOA Flight Test Results: An Overview," SAE Aerospace Atlantic Conference and Exposition, SAE International Paper 931367, Apr. 1993.

[13] Gilbert, W. P., Nguyen, L. T., and Gera, J., "Control Research in the NASA High-Alpha Technology Program," *Aerodynamics of Combat Aircraft Controls and of Ground Effects*, AGARD CP-465, Neuilly sur-Seine, France, Apr. 1990, pp. 3-1–3-18.

[14] Ogburn, M. E., and Foster, J. V., "Development of High-Angle-of-Attack Nose-Down Pitch Control Margin Design Guidelines for Combat Aircraft," NASA CP-10127, Dec. 1993, pp. 293–322.

[15] "Cooperative Program on Dynamic Wind Tunnel Experiments for Maneuvering Aircraft," AGARD Rept. AR305, Neuilly sur-Seine, France, Oct. 1996.

[16] Lutze, F. H., "Analysis of the Falling Leaf Motion Using a Rotational Axes Coordinate System," AIAA Atmospheric Flight Mechanics Conference and Exhibit, Portland, OR, AIAA Paper 1999-4314, Aug. 1999.

[17] Kalviste, J., "Math Modeling of Aero Data for Aircraft Dynamic Motion," AIAA Atmospheric Flight Mechanics Conference, AIAA Paper 94-AFM-26-7, Aug. 1994.

[18] Stevens, B. L., and Lewis, F. L., *Aircraft Control and Simulation*, Wiley, New York, 1992.

[19] Miele, A., *Flight Mechanics Volume 1 Theory of Flight Paths*, Addison–Wesley, London, 1962.

[20] Roskam, J., *Airplane Flight Dynamics and Automatic Flight Controls*, Pt. 1, DARcorporation, Lawrence, KS, 2003.

[21] Shamma, J. S., and Athans, M., "Gain-Scheduling: Potential Hazards and Possible Remedies," *IEEE Control Systems Magazine*, Vol. 12, No. 3, June 1992, pp. 101–107.
doi:10.1109/37.165527

[22] Snell, S. A., and Stout, P. W., "Robust Control of Angle of Attack Using Dynamic Inversion Combined with Quantitative Feedback Theory," AIAA Guidance, Navigation, and Control Conference, San Diego, CA, AIAA Paper 96-3783, July 1996.

[23] Snell, S. A., Enns, D. F., and Garrard, W. L., "Nonlinear Inversion Flight Control for a Supermaneuverable Aircraft," *Journal of Guidance, Control, and Dynamics*, Vol. 15, No. 4, July–Aug. 1992, pp. 976–984.
doi:10.2514/3.20932

[24] Bugajski, D. J., and Enns, D. F., "Nonlinear Control Law with Application to High Angle-of-Attack Flight," *Journal of Guidance, Control, and Dynamics*, Vol. 15, No. 3, May–June 1992, pp. 761–767.
doi:10.2514/3.20902

[25] Smith, P. R., "Functional Control Law Design Using Exact Non-Linear Dynamic Inversion," AIAA Atmospheric Flight Mechanics Conference, AIAA Paper 94-3516-CP, Aug. 1994, pp. 481–486.

[26] Smith, P. R., and Patel, Y., "Translational Motion Control Of VSTOL

Aircraft Using Nonlinear Dynamic Inversion," AIAA Atmospheric Flight Mechanics Conference, AIAA Paper 95-3452-CP, Aug. 1995, pp. 238–252.

[27] Ostroff, A. J., and Bacon, B. J., "Force and Moment Approach for Achievable Dynamics using Nonlinear Dynamic Inversion," AIAA Guidance, Navigation, and Control Conference, AIAA Paper 99-4001, Aug. 1999.

[28] Enns, D., Bugajski, D., Hendrick, R., and Stein, G., "Dynamic Inversion: An Evolving Methodology for Flight Control Design," *International Journal of Control*, Vol. 59, No. 1, Jan. 1994, pp. 71–91.
doi:10.1080/00207179408923070

[29] Snell, A., "Decoupling Control with Applications to Flight," *Journal of Guidance, Control, and Dynamics*, Vol. 21, No. 4, 1998, pp. 647–655.
doi:10.2514/2.4284

[30] Ito, D., Georgie, J., Valasek, J., and Ward, D. T., "Re-Entry Vehicle Flight Controls Design Guidelines: Dynamic Inversion," Flight Simulation Lab., Texas Engineering Experiment Station, Texas A&M Univ., TR NAG9-1085, College Station, TX, May 2001.

[31] Smith, P. R., and Berry, A., "Flight Test Experience of a Non-Linear Dynamic Inversion Control Law on the VAAC Harrier," AIAA Paper 2000-3914, Aug. 2000.

[32] "Flying Qualities of Piloted Aircraft," U.S. Department of Defense, MIL-STD-1797A, Jan. 1990.

[33] Balas, G. J., Garrard, W. L., and Reiner, J., "Robust Dynamic Inversion Control Laws for Aircraft Control," AIAA Guidance, Navigation, and Control Conference, Hilton Head, SC, AIAA Paper 92-4329, Aug. 1992, pp. 192–205.

[34] Cheng, V. H. L., Njaka, C. E., and Menon, P. K., "Practical Design Methodologies for Robust Nonlinear Flight Control," AIAA Guidance, Navigation, and Control Conference, San Diego, CA, AIAA Paper 96-3785, July 1996.

[35] Papageorgiou, C., and Glover, K., "Robustness Analysis of Nonlinear Flight Controllers," *Journal of Guidance, Control, and Dynamics*, Vol. 28, No. 4, July–Aug. 2005, pp. 639–648.
doi:10.2514/1.9389

[36] Zames, G., "Feedback and Optimal Sensitivity: Model Reference Transformation, Multiplicative Seminorms, and Approximate Inverses," *IEEE Transactions on Automatic Control*, Vol. 26, No. 2, 1981, pp. 301–320.
doi:10.1109/TAC.1981.1102603

[37] Skogestad, S., and Postlethwaite, I., *Multivariable Feedback Control, Analysis and Design*, Wiley, New York, Aug. 2001.

[38] Doyle, J., "Analysis of Feedback Systems with Structured Uncertainties," *IEE Proceedings Part D, Control Theory and Applications*, Vol. 129, No. 6, Nov. 1982, pp. 242–250.
doi:10.1049/ip-d:19820053

[39] Nalbantoglu, V., "Robust Control and System Identification for Flexible Structures," Ph.D. Thesis, Univ. of Minnesota, Minneapolis, MN, July 1998.

[40] Doyle, J., Wall, J. E., and Stein, G., "Performance and Robustness Analysis for Structured Uncertainty," *Proceedings of the IEEE Control Decision Conference*, Inst. of Electrical and Electronics Engineers, Piscataway, NJ, 1982, pp. 629–636.

[41] Atesoglu, Ö., and Özgören, M. K., "High-alpha Flight Maneuverability Enhancement of a Fighter Aircraft Using Thrust-Vectoring Control," *Journal of Guidance, Control, and Dynamics*, Vol. 30, No. 5, 2007, pp. 1480–1493.
doi:10.2514/1.28620

[42] Garza, F. R., and Morelli, E. A., "A Collection of Nonlinear Aircraft Simulations in MATLAB," NASA TM-2003-212145, Jan. 2003.

[43] Nguyen, L. T., Ogburn, M. E., Gilbert, W. P., Kibler, K. S., Brown, P. W., and Deal, P. L., "Simulator Study of Stall/Post-Stall Characteristics of a Fighter Airplane with Relaxed Longitudinal Static Stability," NASA Langley Research Center TP 1538, Hampton, VA, 1979.

[44] Titterton, M. C., and Weston, J. L., *Strapdown Inertial Navigation Technology*, 2nd ed., Inst. of Electrical and Electronics Engineers, Piscataway, NJ, 2004, Chap/ 13.

[45] Maybeck, P. S., *Stochastic Models, Estimation, and Control*, Vol. 1, Academic Press, New York, 1979.

[46] Kay, J., Mason, W. H., Durham, W., and Lutze, F., "Control Authority Assessment in Aircraft Conceptual Design," AIAA Paper 93-3968.

[47] Williams, J. E., and Vukelich, S. R., "The USAF Stability and Control DATCOM," U.S. Air Force Flight Dynamics Lab., TR-79-3032, Vol. 1, Wright–Patterson AFB, OH, Apr. 1979.